



Spectral Tuning, Stabilities under External Exposures, and Spontaneous Enhancement of Emission Intensity in Grown-into-Glass All-Inorganic Metal Halide Perovskite Nanocrystals

Fengwen Kang, Yongping Du, Ze Yang, Philippe Boutinaud, Martijn Wubs, Jie Xu, Haiyan Ou, Dongzhe Li, Kaibo Zheng, Abebe T Tarekegne, et al.

► To cite this version:

Fengwen Kang, Yongping Du, Ze Yang, Philippe Boutinaud, Martijn Wubs, et al.. Spectral Tuning, Stabilities under External Exposures, and Spontaneous Enhancement of Emission Intensity in Grown-into-Glass All-Inorganic Metal Halide Perovskite Nanocrystals. *Laser and Photonics Reviews*, 2022, pp.2200166. 10.1002/lpor.202200166 . hal-03825188

HAL Id: hal-03825188

<https://hal.science/hal-03825188>

Submitted on 22 Oct 2022

HAL is a multi-disciplinary open access archive for the deposit and dissemination of scientific research documents, whether they are published or not. The documents may come from teaching and research institutions in France or abroad, or from public or private research centers.

L'archive ouverte pluridisciplinaire **HAL**, est destinée au dépôt et à la diffusion de documents scientifiques de niveau recherche, publiés ou non, émanant des établissements d'enseignement et de recherche français ou étrangers, des laboratoires publics ou privés.

Spectral Tuning, Stabilities under External Exposures, and Spontaneous Enhancement of Emission Intensity in Grown-into-Glass All-Inorganic Metal Halide Perovskite Nanocrystals


Fengwen Kang,* Yongping Du, Ze Yang, Philippe Boutinaud, Martijn Wubs, Jie Xu, Haiyan Ou, Dongzhe Li, Kaibo Zheng, Abebe T. Tarekegne, Guohuan Sun, Xuhui Xu,* and Sanshui Xiao*

Herein, the grown-into-glass (GIG) $\text{CsPbBr}_3\text{:Ln}^{3+}$ ($\text{Ln} = \text{La}, \text{Lu}$) nanocrystals (NCs) are designed and fabricated using an in situ nanocrystallization method. It is shown that a substitution of Pb^{2+} sites with Ln^{3+} ions leads to a blueshift of emission position induced by an increase of the bandgap of CsPbBr_3 . Additionally, the GIG-samples are revealed to feature excellent photoluminescent (PL) properties after being immersed respectively in water for 300 days at room temperature, boiling water for 12 h, and corrosive environments for 24 h, as well as recoverable PL intensity either after several cycles of heat-cooling experiments or after being continuously exposed to a 405 nm laser irradiation. Besides, a spontaneous enhancement of 20–25% of emission intensity during the 1–2.5 hours' stage of a 405 nm laser irradiation, attributed to the radiative recombination of charge carriers that can be de-trapped from trapping levels upon the laser light irradiation and that then spontaneously reinforces the emission intensity, is observed in the GIG- $\text{CsPbBr}_3\text{:Ln}^{3+}$ NCs. Finally, a white light-emitting prototype, with a CIE chromaticity coordinate at (0.4110, 0.3706), a color rendering index of 89 and a correlated color temperature of 3363 K is realized by combining the GIG- CsPbBr_3 NCs, YAG:Ce and $\text{CaWO}_4\text{:Eu}$ phosphors.

1. Introduction

Recently, all-inorganic metal halide perovskites (MHPs) ABX_3 ($\text{A} = \text{Cs}, \text{CH}_3\text{NH}_3, \text{CH}(\text{NH}_2)_2$; $\text{B} = \text{Sn}, \text{Pb}$; $\text{X} = \text{Cl}, \text{Br}, \text{I}$), quaternary lead-free halide double perovskites $\text{A}_2\text{B}'\text{B}''\text{X}_6$ ($\text{A} = \text{CH}_3\text{NH}_3, \text{Cs}$; $\text{B}' = \text{Na}, \text{K}, \text{Cu}, \text{Ag}, \text{Tl}$; $\text{B}'' = \text{In}, \text{Bi}, \text{Sb}$; $\text{X} = \text{Cl}, \text{Br}, \text{I}$), lead- or halide-free yet oxygen-contained $\text{A}_2\text{B}'\text{B}''\text{O}_6$ perovskites, and their hybrid derivatives,^[1–9] have been receiving great attention and are now a hot research subject in many scientific fields for their exceptional optoelectronic and physicochemical properties such as narrow emission bandwidth, broad spectral tuning range, high color purity and brightness, and good light absorption efficiency.^[1–3,5,7,9] Meanwhile, as a result of numerous preparation routes developed over the past years (e.g., laser-assisted irradiation treatment, solid-state reaction, coprecipitation, electrochemical method,

F. Kang^[+], M. Wubs, H. Ou, A. T. Tarekegne, S. Xiao
DTU Fotonik
Department of Photonics Engineering
Technical University of Denmark (DTU)
Lyngby 2800 Kongens, Denmark
E-mail: kangfengwen0597@126.com; saxi@fotonik.dtu.dk

 The ORCID identification number(s) for the author(s) of this article can be found under <https://doi.org/10.1002/lpor.202200166>

^[+]Present address: College of Materials Science and Engineering, Sichuan University, Yihuan Road No. 24 South Section 1, Chengdu, Sichuan 610065, P. R. China

© 2022 The Authors. Laser & Photonics Reviews published by Wiley-VCH GmbH. This is an open access article under the terms of the Creative Commons Attribution License, which permits use, distribution and reproduction in any medium, provided the original work is properly cited.

DOI: 10.1002/lpor.202200166

F. Kang^[+]
Laboratory of Advanced Nano Materials and Devices, Institute of Materials Technology (IMT)
Ningbo Institute of Materials Technology and Engineering (NIMTE)
Chinese Academy of Sciences (CAS)
Ningbo 315201, P. R. China

Y. Du
Center for Nanostructured Graphene
and DTU Physics
Technical University of Denmark
Kongens Lyngby 2800 Kongens, Denmark

Z. Yang, X. Xu
Faculty of Materials Science and Engineering
Kunming University of Science and Technology (KUST)
Wenchang Road, Kunming 650093, China
E-mail: xuxuh07@126.com

P. Boutinaud
Université Clermont Auvergne
Clermont Auvergne INP
CNRS
ICCF
Clermont-Ferrand F-63000, France

self-assembly, sol–gel and wet-chemical approach, hydrothermal and solvothermal routes, and a coupled arrangement of these strategies^[1–3,5,6,8,10], a variety of perovskite-structured materials (PMs) featuring different particle sizes and morphologies have become available, and they are now widely suggested for use in biological purpose, micro- and nanolaser, X-ray scintillation, information encryption and decryption, optical encoding and sensing, 3D nanoprinting, solid-state lighting technology like white LEDs and backlight display, solar cells, and photo- or electrocatalytic purposes.^[3–13] However, the disadvantages of PMs, MHPs in particular, are that they always suffer from the structural and optical instabilities under external exposures like oxygen, moisture, corrosive chemicals like strong alkaline and acid solutions, heat and light, which consequently limit the application scopes and future development.

To address the above-mentioned problems, numerous attempts and efforts have been made over the past years to sustain the properties of the PMs.^[5,10,14–23] These feasible strategies include the compositional engineering,^[14] shielding the PMs either with a layer like the polymer PMMA,^[15] SiO₂,^[16,17] or with a component-matched regulation,^[18] surface modification through using adhesion ligands^[5,19] or repairing surface traps,^[20] and forming a hybrid structure.^[21] However, these strategies also contain some potential disadvantages that cannot be addressed well by themselves, typically when the MHPs are continuously exposed for a quite long-term in the extreme external conditions including ultrahigh and ultralow temperature, and strong corrosive acid and alkaline chemicals. Engineering A- and B-sites in the ABX₃-typed MHPs through appropriately doping external ions is known to enhance the photocharge carrier transport capability^[22] and modify the self-trapped excited states caused by lattice deformation.^[23] However, it may not solve the structural and photoluminescent (PL) instabilities radically since the MHPs compounds are still exposed to external environments and in principle, thus, would not avoid contacting the oxygen, moisture, and chemical agents. Covering the MHPs with a chemi-

cal agent or ligand, inert structure-matched shells, polymer matrix, and oxides-based layers was demonstrated to improve the properties, but the surface protection layers, as exemplified by their transmission electron microscopy (TEM) or SEM images in the archival literatures,^[5,10,14–24] holds only several or a few tens of nano-/micrometers after roughly evaluating from the bottom edge of the layers. This unfortunately means that they may not be thick enough to fully protect the MHPs and their relevant PL properties from the aforementioned harsh external conditions. Moreover, in most cases, a surface structure-matching method always results in intrinsically unstable or incomplete coating shells, while coating with organic polymers like polymethyl-methacrylate and polystyrene is susceptible to high temperature or high-power light irradiation damage.^[25] Furthermore, a recent work stated that dispersing the MHPs into organic solvents like acetone^[11] sustains their PL properties and particles' dispersion, but it leads to a severe decrease in the PL intensity due to the particles' agglomeration once they are extracted from these organic solutions. Apart from the above aspects, the PMs particles that were initially fixed individually at different locations may also randomly diffuse, be agglomerated, and even be coagulated upon, for instance, a repeated thermal stimuli, no matter whether or not they are crystallized in regular morphologies and size. Moreover, using the oxides-based inorganic coating layers such as SiO₂^[16,17,26–28] leads to better stabilities of MHPs as compared to the counterparts without coating. However, since the SiO₂ belongs to a type of mesoporous material,^[24,28] the gradual degradation of the PL and/or structural properties of the MHPs may appear after staying in air for a long term due to moisture. In terms of the analysis we mentioned or deduced above, keeping the PMs well-dispersed and distant enough one from others (the MHPs in particular) is a matter of importance to prevent the structural and PL stabilities from being affected by external exposures. This also indicates that such issues, if they cannot be addressed well, would worsen the PL and/or structural properties of PMs and thus, are not good for and may even be detrimental to, such as, the lighting device fabrication.^[11]

During the last three to five years, strategies involving the growth and stabilization of MHPs nanocrystals (NCs) like CsPbBr₃ into a glass matrix by use of an in situ crystallization route^[29] or postmelting procedure^[30] have demonstrated great improvements in terms of luminescent quantum yields, water-resistance, thermal- and long-term photostability in comparison with the glass-unprotected (hereafter GU) counterparts.^[12,29–34] The benefits in these concerns are, on the one hand, to keep the NCs particles away from each other and/or from the glass edge and may, on the other hand, sustain the optimized micro- or nanostructure under external exposures for a relative long term. That is, each MHPs particle crystallized in the glass matrix is expected to keep a relatively fixed location in the glass matrix, without being moved around easily with the change of the external environments such as thermal stimuli. Note here that the temperature of the thermal stimulus mentioned is well below the transition temperature (T_g) of the glass itself. As compared to GU-MHPs and those improved by coating SiO₂, PMMA, adhesion ligands or polymers on the MHPs surfaces, it is clear that the glass-stabilized method shows the potential in minimizing the risks of particle agglomeration and may thereby be treated as a feasible strategy to sustain the PL properties of the MHPs

J. Xu
School of Medical Information and Engineering
Southwest Medical University
Luzhou 646000, China

D. Li
CEMES
Université de Toulouse
CNRS
29 rue Jeanne Marvig, Toulouse F-31055, France

K. Zheng
Department of Chemistry
Technical University of Denmark (DTU)
Lyngby 2800 Kongens, Denmark

K. Zheng
Department of Chemical Physics and NanoLund
Lund University
Lund 22100, Sweden

G. Sun
State Key Laboratory of Experimental Hematology (SKLEH), Haihe
Laboratory of Cell Ecosystem, National Clinical Research Center for
Blood Diseases
Institute of Hematology and Blood Diseases Hospital
Chinese Academy of Medical Sciences and Peking Union Medical College
Tianjin 300020, P. R. China

NCs for longer periods of time. For example, Yuan et al.^[33] reported that in comparison to the colloidal GU-CsPbBr₃ quantum dots (QDs) that lost ≈95% of the PL intensity after being immersed in water for 2 h, the CsPbBr₃ QDs embedded into a CeO₂-based glass matrix show especially that the PL intensity of the glass-protected sample remains ≈90% of the initial PL intensity after being immersed in water for 120 h at room temperature (RT). Huang et al.^[31,32] found that the CsPbBr₃ NCs inside a transparent glass medium feature reversible PL intensity, spectral bandwidths, and peak positions after several cycles of switching on and off a 365 nm UV light, and revealed further that these glass-protected CsPbBr₃ NCs sustain bright green color after being kept in deionized water and ethanol for 30 and 60 days, respectively. In these works, the distances separating the CsPbBr₃ particles from the glass edge, as roughly evaluated by their TEM images, amount tens to hundreds of nanometers and even up several micrometers. We are thus inspired by these brief surveys that protecting the MHPs by a glass constitutes a particularly desirable strategy for sustaining the relevant PL properties by, on the one hand, promoting a statistical dispersion (i.e., minimizing the accumulation probabilities) of the MHPs NCs and, on the other hand, preventing a direct contact with external environments. Besides, MHPs with an inherent ionic structure like the CsPbBr₃ appear furthermore as the relevant achievable candidates in the glass matrix are due to a relatively low formation energy,^[31,35] which permits easy nucleation and growth in a suitable glass matrix. For this reason, the crystallization and growth of the CsPbBr₃ NCs as reported by Huang et al.^[31,32] can be controlled using a high-energy femtosecond laser that combines the laser light irradiation and the thermal annealing stimuli, leading to encapsulated controllable patterns. These encouraging results prompted us to select this in situ crystallization route to prepare the grown-into-glass (GIG) CsPbBr₃ NCs.

As known, bulk MHPs (BMHPs) with a given structural composition and particle size usually show relatively simple spectroscopic properties upon excitation at a given wavelength, including a fixed emitting-color due to the fixed PL intensity and position, PL quantum yields, and spectral bandwidth. To improve and enrich the PL properties, significant efforts have been made, and they have led to the remarkably tunable optical properties that result either from managing the isostructural perovskite systems, or from doping and/or codoping with rare-earth (RE) (e.g., Eu³⁺, Eu²⁺, Pr³⁺, Sm³⁺, Gd³⁺, Dy³⁺, Ce³⁺, Yb³⁺, Er³⁺, Tb³⁺) and non-RE (e.g., Bi³⁺, Cu²⁺, Mn⁴⁺, Mn²⁺, Ni²⁺, Cr³⁺, Mg²⁺, Zn²⁺) ions, as well as from controlling the energy transfer process among these absorbing and emitting species.^[3,5,36–49] Among them, multicolor tuning sometimes can be achieved through adjusting the relative emission intensity between different dopants or between the PMs and the dopants in, for instance, CsPbCl₃:Mn²⁺,^[38] Ba₂GdNbO₆:Bi³⁺,Mn⁴⁺,^[40] and Cs₂AgInCl₆:Bi³⁺ NCs,^[42] and Ca₂MgWO₆:Cr³⁺,Yb³⁺.^[48] In particular, in the case of an efficient energy transfer from BMHPs to dopants, the final emissions are dominated by the non-RE and/or RE ions, such as, in the Mn²⁺-doped (But)₂PbBr₄ NCs^[49] and Cr³⁺-doped Cs₂AgInCl₆ NCs.^[50] Moreover, due to the atomic-like behaviors, some RE- or non-RE-doped BMHPs only exhibit the unchanged spectral positions and thus emit the fixed colors accordingly, as for example, in the Sm³⁺-, Eu³⁺-, Tb³⁺-, Dy³⁺-, Er³⁺-, and Yb³⁺-doped CsPbCl₃ NCs,^[39] Mn²⁺-doped

CsPbCl₃,^[51] or Tb³⁺-doped CsPbI₃ NCs.^[52] In these works, the RE and non-RE dopants serve as the luminescent activators, but their combination with MHPs always suffer from the light reabsorption issues due to the spectral overlap between their emission and excitation/absorption bands, or the color imbalance that results from different responses of different activators to, such as, the same temperature. This is well illustrated in the Ba₂GdNbO₆:Bi³⁺,Mn⁴⁺,^[36] (C₈H₂₀N₂)PbBr₄:Mn²⁺,^[53] and CsPbCl_{3-x}Br_x:Mn²⁺ (x = 2.8%) NCs^[54] that show a different PL intensity reduction between Bi³⁺ and Mn⁴⁺ ions, Mn²⁺ ions and (C₈H₂₀N₂)PbBr₄, and Mn²⁺ ions and CsPbCl_{3-x}Br_x (x = 2.8%) as the temperature is increased from 77 to 300 K, 7 to 400 K, and 4.2 to 300 K, respectively. Such innate shortcomings, in principle, can however be addressed if the selected dopants are not used for their inner luminescent properties but for their aptitude to modify the luminescence of the host cell lattice that welcomes it. As exemplified by Pan et al.^[39] in Ce³⁺, Sm³⁺, Eu³⁺, Tb³⁺, Dy³⁺, Er³⁺, and Yb³⁺ doped CsPbCl₃ NCs, and Begum et al.^[55] in Bi³⁺-doped CsPbBr₃ NCs, the dopants do not exhibit their luminescence but modify the spectroscopic properties of CsPbCl₃ and CsPbBr₃ NCs. The same scenarios are also seen in two recent works that concern the Lu³⁺, Tb³⁺, Pr³⁺, La³⁺, and Eu³⁺ doped GIG-CsPbBr₃ NCs.^[34,56]

Following the above observations and considerations, we have prepared a series of MHPs-typed GIG-CsPbBr₃ NCs either undoped or doped with nonluminescent La³⁺ and Lu³⁺ ions by means of an in situ nanocrystallization method. Our aim is threefold.

- 1) Investigate the PL properties' change of GIG-CsPbBr₃:Ln³⁺ (Ln = La, Lu) NCs and identify the corresponding working principles that are not perturbed by the inner optical properties of the Ln³⁺ dopants. In this concern, the nonluminescent La³⁺ and Lu³⁺ ions caught our eyes and were selected for their relatively high contrast of ionic radii among trivalent lanthanides. Accordingly, their incorporation in the CsPbBr₃ cell lattice is expected to affect the CsPbBr₃ cell lattice and then modulate the corresponding PL properties with the largest amplitude, which, as we will see, can be evidenced by a blueshift of PL positions that is amplified as the doping rates of La³⁺ or Lu³⁺ ions are raised in the GIG-CsPbBr₃:Ln³⁺ NCs. Based on the spectroscopic analysis combined with the structural discussion and density functional theory (DFT) calculation, this spectral shift is assigned to a modulation of the optical bandgap energies.
- 2) Qualify the PL behavior of GIG-CsPbBr₃, GIG-CsPbBr₃:Ln³⁺, and GU-CsPbBr₃ NCs after being exposed directly to a variety of external harsh conditions like moisture, corrosive chemicals, repeated cycles of heating-cooling experiments, and a 405 nm focused laser light. Specifically, the influence of moisture on the PL properties will first be evaluated by immersing the obtained samples in: i) water in the temperature range of 25–100 °C, and ii) aqueous solutions featuring pH values over the range of 1–14 for tens of hours. The temperature-dependent PL depreciation of MHPs has been summarized^[5,37] and studied by the research works,^[11,28,31,33,39,41,53,54,56] but these previous experiments either involved limited heating-cooling cycles or involved only one heating cycle. As evidenced by GIG-CsPbBr₃ QDs^[33]

and some oxide-based luminescent phosphor materials like $\text{LuVO}_4:\text{Bi}^{3+}$ ^[57] and X2-Type $\text{Y}_2\text{SiO}_5:\text{Eu}^{3+}, \text{Bi}^{3+}$ ^[58] the recoverable PL properties can be achieved in a certain temperature range after one heating–cooling cycle, but this does not mean that the increase of the heating–cooling cycles or the change of the heating–cooling temperature range can still maintain the unrecoverable PL properties. For example, it is reported by Meijerink and co-workers^[59] that the PL intensity of organically capped CdSe QDs incorporated in PMMA retains $\approx 80\%$ of the initial PL intensity in the first heating and cooling cycle (i.e., $+25^\circ\text{C} \leftrightarrow +120^\circ\text{C}$), but it keeps $<40\%$ with a subsequent heating–cooling cycle of $+25^\circ\text{C} \leftrightarrow +160^\circ\text{C}$. In addition, the colloidal CsPbBr_3 QDs in water were found to feature a basically recoverable PL intensity after a heating–cooling experiment cycle in a relatively low temperature range of $+20^\circ\text{C} \leftrightarrow +100^\circ\text{C}$,^[33] but only $\approx 40\%$ and $<10\%$ of the PL intensity retained when the heating–cooling temperature ranges were changed into $+20^\circ\text{C} \leftrightarrow +150^\circ\text{C}$ and $+20^\circ\text{C} \leftrightarrow +200^\circ\text{C}$, respectively. In view of these, we therefore have in situ collected and studied the PL spectra of GIG- CsPbBr_3 and GIG- $\text{CsPbBr}_3:\text{Ln}^{3+}$ NCs in an unchanged temperature range of $-150^\circ\text{C} \leftrightarrow +150^\circ\text{C}$, with up to 30 of the heating–cooling cycles. Meanwhile, the effect of the incoming laser light irradiation on the PL depreciation was also evaluated by focusing a 405 nm laser light onto the surface of the samples for up to 80 h.

- 3) Realize the warm-white emitting output by combining the light of a 405 nm laser with the emissions from green GIG- CsPbBr_3 powders, yellow $\text{YAG}:\text{Ce}^{3+}$ and red $\text{CaWO}_4:\text{Eu}^{3+}$ phosphors. Through evaluating the performances, a near-warm white-emitting prototype, with a CIE chromaticity coordinate at (0.343, 0.3780), high color rendering index (CRI) of 89, and low correlated color temperature (CCT) of 3363 K, is realized, thereby showing the potential of GIG-MHPs toward laser lighting technology.

2. Experimental Section

2.1. Synthesis and Evaluation of the Samples

GIG- $\text{CsPbBr}_3:x\text{La}^{3+}$ and - $\text{CsPbBr}_3:y\text{Lu}^{3+}$ NCs (where $x, y = 0; 0.5\% \leq x, y \leq 1.3\%$, for several x and y values varying by steps of 0.2 mol%) were prepared using a melting–quenching route followed by a subsequent nucleation and growth nanocrystallization in a transparent borosilicate-based glass matrix,^[34] as described in Figure 1a. More specifically, according to the nominal chemical compositions consisting of the amorphous glassy phase medium ($35\text{B}_2\text{O}_3-35\text{SiO}_2-13\text{ZnO}-2\text{SrCO}_3$) and all-inorganic MHPs $9\text{Cs}_2\text{CO}_3-(3-x)\text{PbBr}_2-3\text{NaBr}-x\text{Ln}_2\text{O}_3$ formula (where the x and y values are the mole percentage and, in terms of the previous works,^[33,34] the Ln^{3+} dopants are assumed to substitute the Pb^{2+} lattice sites), the raw chemicals of SiO_2 (99.99%), ZnO (99.9%), B_2O_3 (99.9%), SrCO_3 (99.99%), Cs_2CO_3 (99.99%), NaBr (99.99%), La_2O_3 (99.99%), PbBr_2 (99.9%), and Lu_2O_3 (99.99%), purchased from Shanghai Aladdin Biochemical Technology Co., Ltd, were first mixed in an agate mortar, and then melted at 1200°C for 15 min in an alumina crucible under air. Later on, the melt was poured onto a 400°C preheated stainless steel plate and pressed using a brass plate to form the

precursor glass medium. After that, the precursor of the glass medium was transferred to a muffle furnace and annealed at 490°C for 10 h to release the residual thermal stress and initiate the nucleation growth of CsPbBr_3 and $\text{CsPbBr}_3:\text{Ln}^{3+}$. Then, the GIG- CsPbBr_3 and GIG- $\text{CsPbBr}_3:\text{Ln}^{3+}$ NCs vitroceramics were achieved. Finally, all GIG-samples were cut and polished to the optical grade, and some of them were ground as fine powders for the subsequent experimental characterizations and white-emitting prototype realization.

To qualify the PL stabilities of GIG- CsPbBr_3 and GIG- $\text{CsPbBr}_3:\text{Ln}^{3+}$ samples under external exposures including moisture, corrosive chemicals, heat, and laser light, ≈ 0.01 g of the milled glassy powder was dispersed either in 5 mL of distilled water or in alkali and acid solutions, and then kept at RT in air. Approximately 0.05 g of powder was added to 50 mL of distilled water, and gradually heated until boiled. To maintain the total volume, distilled water was also supplemented for evaporation during the boiling process. The optically polished glass was directly used to study the laser-light tolerated PL stability, by focusing a 405 nm laser onto a given glass surface or a fine-milled powder particle.

In parallel, following the synthetic steps developed by Kovalenko et al.^[36] and reused in two of the previous works,^[60,61] GU- CsPbBr_3 NCs were also prepared to illustrate the PL stability properties of GIG-samples from the opposite side. Specifically, 40 mL of 1-octadecene (ODE, Sigma-Aldrich, 90%), 0.814 g of Cs_2CO_3 (Sigma-Aldrich, 99%), and 2.5 mL of oleic acid (OA, Sigma-Aldrich, 90%) were first mixed. Later on, the mixtures were rapidly heated up to 120°C , and then to 150°C for 30 min under an N_2 atmosphere followed by keeping at 120°C for 1 h under a vacuum. After that, Cs-oleate was kept in a glovebox, then heated up to 100°C , and finally kept at this temperature before use. After heating the mixtures formed by 0.689 g of PbBr_2 (Sigma-Aldrich, 99.999%) and 10 mL of ODE for 120°C under vacuum for 1 h, 0.5 mL of dry oleylamine (OAm, Sigma-Aldrich, 80–90%) and 0.5 mL of OA were added and heated up to 120°C under N_2 atmosphere. Followed by the steps of: i) increasing the temperature of the mixture solutions to 180°C , ii) injecting 0.4 mL of Cs-oleate solutions, and iii) immediately cooling by use of the ice-water bath, the aimed GU- CsPbBr_3 NCs were obtained, and they were suspended in acetone for further use.

2.2. Characterization Details

The XRD patterns of GIG- CsPbBr_3 and - $\text{CsPbBr}_3:\text{Ln}^{3+}$ samples were recorded on a Rigaku D/Max 2200 Powder X-ray Diffractometer operating at 40 kV and 30 mA with $\text{Cu K}\alpha$ radiation ($\lambda = 1.5406 \text{ \AA}$). TEM measurements were done on a Titan Analytical 80–300ST TEM operated with an X-FEG running at 300 kV accelerating voltage. Images were acquired on a Gatan Ultrascan US1000 CCD with 2048×2048 px. Considering the electron beam penetration capability and the beam-sensitive CsPbBr_3 NCs, the TEM images were collected on the thin edge of GIG-samples. In the process of GIG-samples' post-treatment, the powders were first put into deionized water, shaken, left aside, and then used a Pipette to absorb the supernatant and dry-dispersed on a Cu-lacey carbon grid. For the TEM images of GU- CsPbBr_3 NCs, a pipette was used to extract the acetone-suspended GU- CsPbBr_3

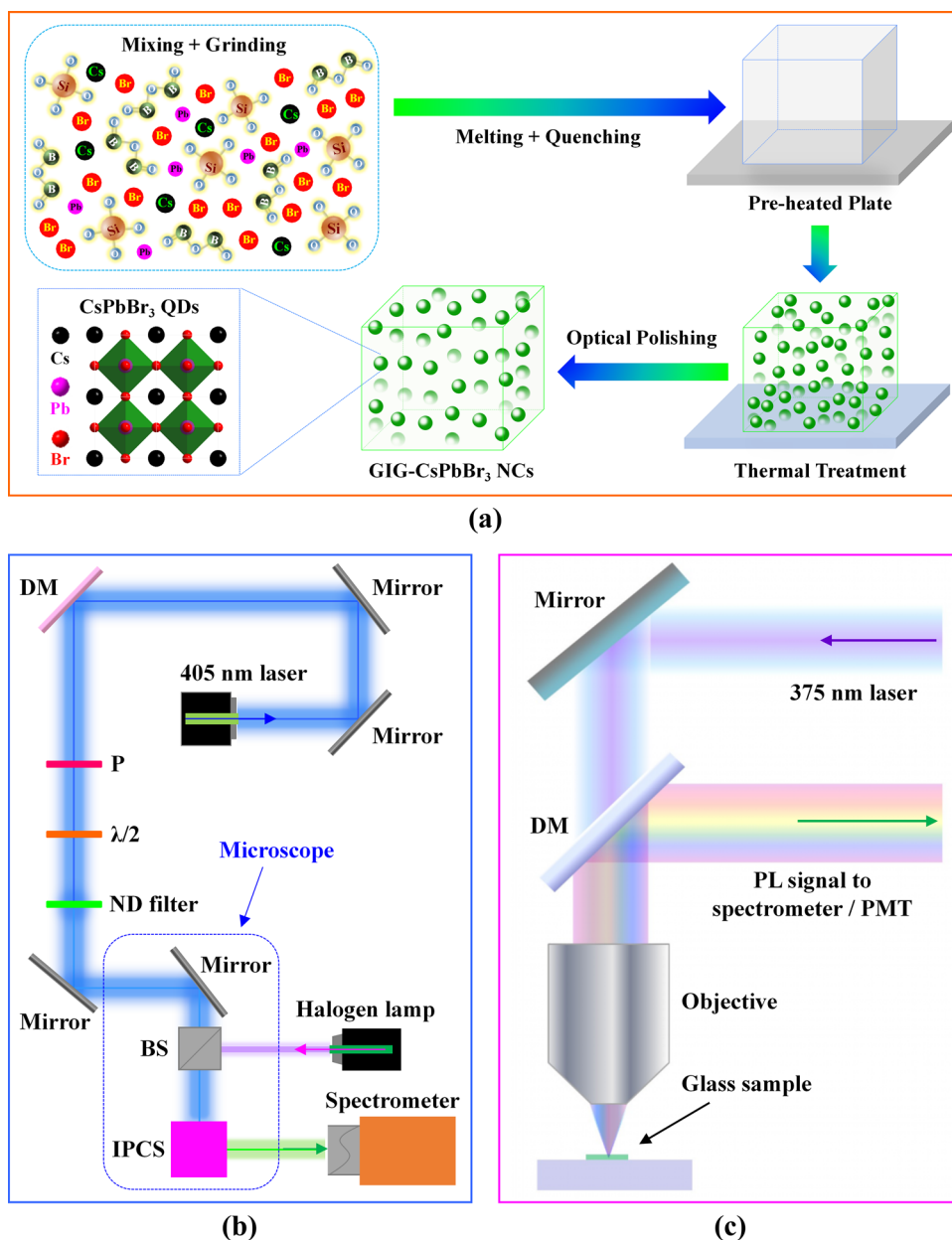


Figure 1. a) Major experimental synthesis steps of GIG-CsPbBr₃:xLn³⁺ (Ln = La, Lu; x, y = 0; 0.5% ≤ x, y ≤ 1.3%) NCs. b,c) Home-built PL data collection systems for measuring RT, heat- and light-tolerated PL spectra upon excitation at a 405 nm (b) and at a 375 nm lasers (c), in which DM is dichroic mirror, IPCS is image processing computer systems, ND is neutral density, and PMT is photomultiplier tube.

NCs (≈200 μL), washed with the ethanol and deionized water two times, and then dry-dispersed on a Cu-lacey carbon grid. The RT, heat-, and light-tolerated PL spectra were collected using a home-built PL data collection system operated with a 405 nm CW laser. The simplified sketch of this PL setup is depicted in Figure 1b. It consists of a halogen lamp with output power spanning from 0 to 100 W, a shamrock 303i spectrometer, a 460 nm long-pass filter (i.e., used for filtering the collected PL signals), a Nikon Ti-U Inverted Microscope (which can be used for bright-field reflection), and a bright-field transmission. The heating-cooling PL measurements were in situ recorded on a UK THMS600 Linkam device coupled to the Nikon Ti-U inverted Microscope, with a

heating-cooling rate of 150 °C min⁻¹ over the temperature range of -150 ↔ +150 °C, a focused laser spot (here the objective of a Nikon 50× TU Plan APO was used) on a fixed surface of the samples, and a fixed slit (e.g., 150 μm), as well as the identical parameters (e.g., an exposure time of 0.01 s, and the number of accumulations of 10). For the light-tolerated PL spectra, the samples were exposed continuously to a focused 405 nm laser beam for up to 80 h. The measurements of the laser-induced PL enhancement and subsequent PL depreciation were performed under continuous irradiation of a 405 nm laser. The samples were all irradiated continuously under the laser light for tens of hundreds of hours, without the laser off. When the irradiation time

reached 3 h, for example, the spectrometer was then turned on and started to measure the PL spectra. For the laser cut-off process, the samples were continued to be kept in the sample chamber. Once the cut-off time come to a given time like 10 h, the laser was turned off and then the spectrometer started to measure the PL spectra. The measurement time used for collecting each PL enhancement and depreciation data was comparatively short, just 0.01 s. Additionally, the RT PL spectra of the samples upon excitation with a 375 nm CW laser were also collected, but the PL data collection system, as depicted in Figure 1c, differed in that of Figure 1b. This setup used a single microscope objective (NA = 0.8) for the PL collection. The collected PL signals were transmitted through a 405 nm long-pass filter and fiber-coupled to an optical spectrometer (SR-3031-A spectrograph with DU-420-OE CCD). The effects of external exposures (i.e., water at RT, boiling water, and corrosive chemicals with the pH values over the range of 1–14) on the PL properties of samples were recorded on a Hitachi F-7000 fluorescent spectrophotometer equipped with a Xe lamp as an excitation source. The details of other experimental treatments that were not described here will be seen in the below text.

3. Theoretical Details

Our first-principles calculations were performed within the framework of DFT using the Vienna ab initio simulation package (VASP).^[62] A kinetic energy cutoff of 400 eV was used for the plane wave basis set expansion and Brillouin zone integration was performed on a regular mesh of $13 \times 13 \times 13$ *k*-points for the bulk self-consistent calculations. Electronic and lattice dynamical properties were calculated with projector-augmented plane-wave potentials^[63] with the generalized gradient approximation (GGA) of Perdew–Burke–Ernzerhof parametrization.^[64] The total energy and forces were converged to smaller than 10^{-7} eV and 10^{-2} eV Å⁻¹ during the structural relaxation. To calculate the doping effect, we also adopted the virtual crystal approximation method implemented in VASP. Note that for the doped materials, we did not include the excitonic and electron–phonon coupling effects in the present calculations.

4. Results and Discussion

4.1. Structural and Microstructural Analysis of Samples

Representative X-ray diffraction (XRD) patterns of GIG-CsPbBr₃ and GIG-CsPbBr₃:0.5%Ln³⁺ (Ln = La, Lu) samples are shown in Figure 2a. They confirm that the major 2 θ -reflection peaks at the planes (110), (200), (211), and (220) agree with that of Inorganic Crystal Structure Database (ICSD) file no. 29073. Referring to those earlier works dedicated to CsPbBr₃-related glass nano-vitroceraics^[12,25,33,34,65–90] and relevant XRD data that we recompiled into Table 2, it seems that the cubic phase is preferred for CsPbBr₃ crystallized in glass matrix. Nevertheless, we cannot fully exclude the form of an orthorhombic distortion in the perovskite lattice and the possible existence of a very small percentage of orthorhombic phase-typed CsPbBr₃ NCs based upon our experimental XRD patterns, so that these issues still remain open in the GIG-MHPs-typed NCs vitroceraics at this stage.

We note from Table 2 that the major 2 θ -reflection positions of CsPbBr₃ NCs differ somehow from one glass system to the other mainly due to the factors such as the types of dopant used, the glass transition and/or crystallization temperature, the thermal treatment duration, or the raw chemical reagents used for forming the glass. We also notice that the major 2 θ -reflection positions of GIG-CsPbBr₃ NCs follow the Vegard's law after being doped with La³⁺ or Lu³⁺ ions (Table 2), in agreement with the scenarios depicted by Cheng et al.^[56] that evidence a shift of the major 2 θ -reflection positions toward higher diffraction angles after doping with Eu³⁺ ions. This shift, however, is not very obvious since, on the one hand, only partial the Pb²⁺ ions are replaced by limited amounts (i.e., 0.5 mol%) of La³⁺ and Lu³⁺ ions, leading to a very limited shrinkage of CsPbBr₃ cell lattice. On the other hand, a relatively high signal-to-noise ratio makes it difficult to precisely locate the specific 2 θ -reflection peaks. Furthermore, the broad yet unresolved reflection bands in the range of 17°–35° are also observed in the GIG-samples due to the amorphous glass medium, and they seem unique for almost all of CsPbBr₃-related glass nano-vitroceraics as we compiled in Table 2.

Low-magnification (LM) and high-magnification (HM) TEM images depicted in Figure 2b reveal that GU-CsPbBr₃ NCs feature an average particle size of 9.8 ± 0.3 nm, with a lattice fringe of 0.404 nm for the plane (110). The LM TEM images presented in Figure 2c,d pertain to GIG-vitroceraics, and they reveal that the GIG-CsPbBr₃:1.1%La³⁺ and GIG-CsPbBr₃:1.1%Lu³⁺ NCs are statistically dispersed in the glass medium, with an inner GIG-particles distance amounting from 6 to 15 nm. This indicates that the GIG-NCs particles retain a certain distance from each other. The statistical average sizes of GIG-CsPbBr₃:1.1%La³⁺ and -CsPbBr₃:1.1%Lu³⁺ NCs are 4.3 ± 1.2 and 3.8 ± 0.9 nm, with (111) and (110) plane-related lattice fringes of 0.346 and 0.409 nm, respectively. It is obvious that these lattice fringes are between the maximum and the minimum of the lattice fringes of the CsPbBr₃ NCs in other glass matrices as we listed in Table 2.

4.2. PL Spectra

The GIG-CsPbBr₃ (i–iii) and GU-CsPbBr₃ NCs (v) exhibit bright green colors upon excitation with a 405 nm continuous wave (CW) laser (Figure 3a), no matter whether they are in form of monolithic bulk glass, powders, or immersed in water at RT and suspended in liquid acetone. The emission spectra of GIG-CsPbBr₃ and GIG-CsPbBr₃:Ln³⁺ samples collected upon excitation with a 375 or 405 nm laser are depicted in Figure 3b. Obviously, upon excitation with a 375 nm laser, the positions' shift range (12.8 nm) in the GIG-CsPbBr₃:xLa³⁺ ($x = 0 \rightarrow 1.3\%$, $\lambda_{em} = 506.6 \rightarrow 493.8$ nm) is narrower than that (15.7 nm) in the GIG-CsPbBr₃:yLu³⁺ ($y = 0 \rightarrow 1.3\%$, $\lambda_{em} = 506.6 \rightarrow 490.9$ nm) NCs. Nevertheless, upon excitation with a 405 nm laser (iii,iv), the positions' shift associated with the same variation of La³⁺ and Lu³⁺ doping rates starts from 510.6 nm and ends at 488.0 and 493.5 nm, corresponding respectively to the shift ranges of 22.6 and 17.1 nm. This indicates that the peaks of the emission bands slightly depend on the excitation wavelength, and a blueshift of the PL intensity maxima is evidenced as the La³⁺ and Lu³⁺ doping contents are increased. Additionally, the PL positions of GIG-CsPbBr₃:0.5%La³⁺ NCs upon excitation at 375 nm (i.e.,

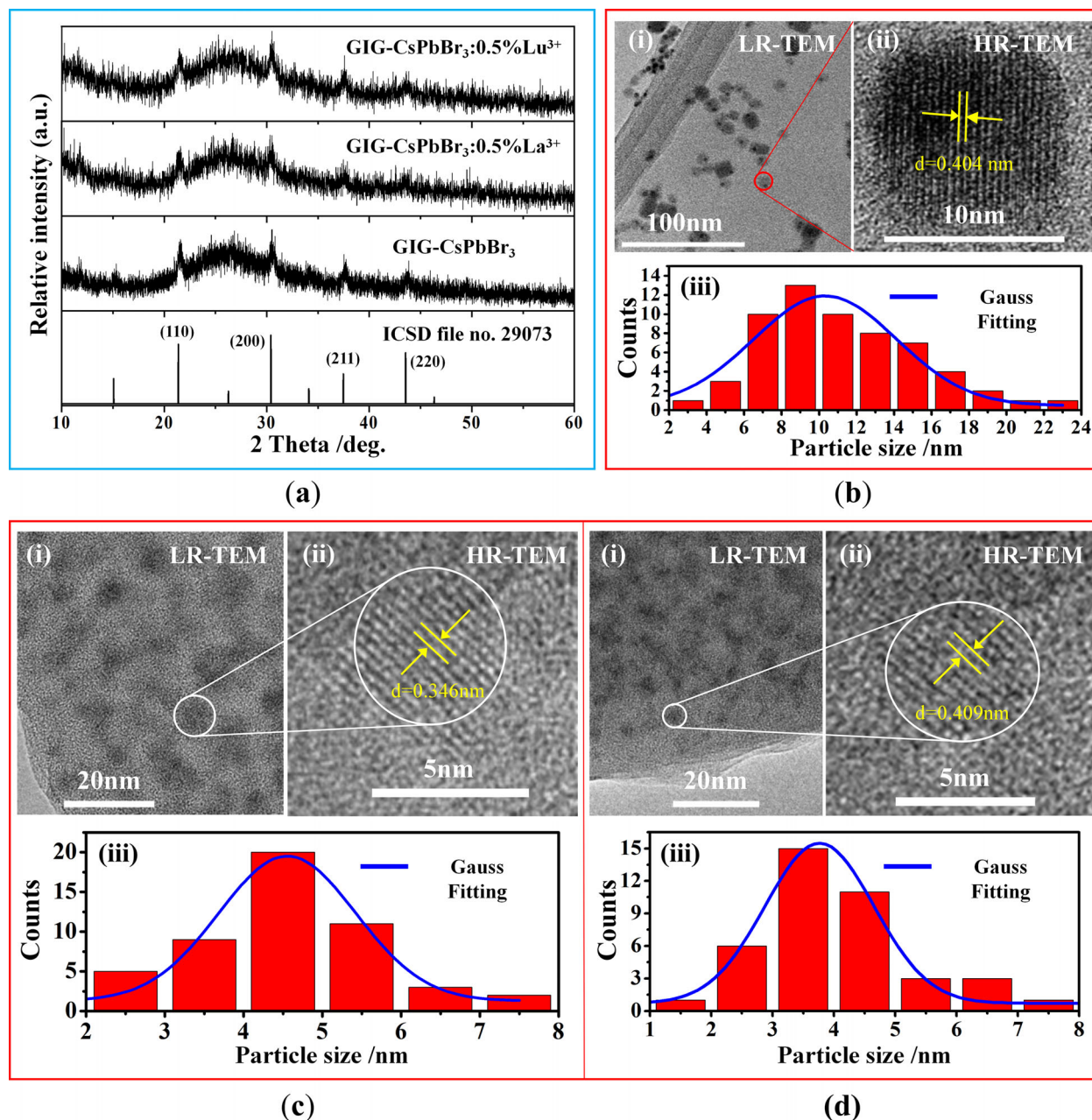


Figure 2. a) XRD patterns of typical GIG-CsPbBr₃:xLn³⁺ (Ln = La, Lu; x, y = 0, 0.5%) NCs. b–d) (i) Low-magnification (LM) and (ii) high-magnification (HM) TEM images and (iii) size distribution of GIG-CsPbBr₃ (b), GIG-CsPbBr₃:1.1%La³⁺ (c), and GIG-CsPbBr₃:1.1%Lu³⁺ (d) NCs. Note that the particle sizes and lattice fringes are directly evaluated by using a Gatan DigitalMicrograph software (version 3.9).

Table 1. Original *a/b/c* parameters from ICSD file no. 29073, DFT-optimized *a/b/c* parameters, and DFT-calculated *E_g* (eV) values of CsPb_xBr₃:xLa³⁺ and CsPb_yBr₃:yLu³⁺.

Dopants	Original <i>a/b/c</i> parameters		DFT-optimized <i>a/b/c</i> parameters, and DFT-calculated <i>E_g</i> values							
	<i>x</i> , <i>y</i> = 0%		<i>x</i> , <i>y</i> = 2%		<i>x</i> , <i>y</i> = 4%		<i>x</i> , <i>y</i> = 6%		<i>x</i> , <i>y</i> = 8%	
	<i>a/b/c</i>	<i>E_g</i>	<i>a/b/c</i>	<i>E_g</i>	<i>a/b/c</i>	<i>E_g</i>	<i>a/b/c</i>	<i>E_g</i>	<i>a/b/c</i>	<i>E_g</i>
La	5.8784	1.7449	5.7825	2.0456	5.7703	2.2210	5.7579	2.3274	5.7160	2.2691
Lu	5.8784	1.7449	5.9960	1.5293	5.9476	1.6758	5.8023	1.8080	5.5118	1.8326

Table 2. Typical CsPbBr₃-related glass reported in the last five years, together with the glass transition temperature (T_g) and crystallization temperature (T_c), CsPbBr₃-assigned crystal system and the referenced XRD card, the major 2θ -reflection position and the corresponding lattice plane, and the particle size, as well as the lattice fringe (d) and the corresponding lattice plane.

Glass matrix/ composition	T_g [°C]	T_c [°C]	NCs	Referenced card	Crystal system	2θ value [°]	Lattice plane	Size [nm]	d [nm]	Plane	Refs.
Zinc–borosilicates	350	450–490	CsPbBr ₃	PDF # 75-0412	Cubic	–	–	5.0	–	–	[12]
Zinc–borosilicates	–	480–520	CsPbBr _{0.252} I _{0.48}	JCPDS # 54-0752	Cubic	–	–	5–10	0.293	(200)	[65]
Phosphosilicates	400	440–450	CsPbBr ₃	PDF # 54-0752	Cubic	21.3	(100)	3.2	0.280	(200)	[66]
						30.4	(200)				
						37.5	(211)				
Borosilicates	450	450–500	CsPbBr ₃	PDF # 54-0752	Cubic	21.31	(100)	–	–	–	[56]
						30.41	(200)				
						37.51	(211)				
			CsPbBr ₃ :Tb ³⁺		Cubic	20.6848	(100)	5.73	0.180	(200)	
						21.1365	(200)				
						21.0675	(211)				
TeO ₂ -based boroaluminates	–	200–400	CsPbBr ₃	JCPDS # 54-0752	Cubic	–	–	6–10	0.291	(200)	[33]
Zinc–borosilicates	420	500	CsPbBr ₃ :La ³⁺	JCPDS # 54-0752	Cubic	–	–	5.7	0.287	(200)	[34]
								–	0.290	(200)	
Zinc–borosilicates	350	450–490	CsPbBr ₃	PDF # 75-0412	Cubic	–	–	5.2	0.228	(211)	[25]
Borosilicates	420	520	CsPbBr ₃	JCPDS # 54-0752	Cubic	21.86	(100)	–	0.295	(200)	[67]
						30.81	(200)				
						34.65	(210)				
						37.92	(211)				
						44.11	(220)				
			CsPbBr ₃ :3.18%Eu ³⁺			–	–	–	0.296		
Phosphosilicates	–	300	CsPbBr ₃	JCPDS # 54-0752	Cubic	–	–	8–15	0.290	(200)	[68]
Zinc–boroantimonates	–	300–400	CsPbBr ₃	JCPDS # 54-0752	Cubic	–	–	3–8	0.238	(211)	[69]
Borogermanates	350	420	CsPbBr ₃	JCPDS # 75-0412	Cubic	–	–	7.9 ± 0.65	0.402	(011)	[70]
Zinc–borosilicates	420	500	CsPbBr ₃	JCPDS # 54-0752	Cubic	–	–	12	0.300	(200)	[71]
			CsPbBr ₃ :Zn					6.5	0.283		
Phosphate	–	>500	CsPbBr ₃	JCPDS # 54-0752	Cubic	–	–	–	0.283	(200)	[72]
Boro-germanates	400	450–520	CsPbBr ₃	JCPDS # 54-0752	Cubic	–	–	6–10	0.410	(110)	[73]
Multicomponent borates	470	490–550	CsPbBr ₃	JCPDS # 54-0752	Cubic	–	–	5–10	0.28	(200)	[74]
									0.26	(210)	
Borosilicates	410	440–530	CsPbBr ₃	PDF # 54-0742	Cubic	–	–	5.64– 7.61	0.209	(220)	[75]
									0.240	(211)	
									0.292	(200)	
Borosilicates	360	475	CsPbBr ₃	PDF # 54-0742	Cubic	21.551	(110)	5.2	0.292	(200)	[76]
						30.645	(200)				
Borosilicates	–	430	CsPbBr ₃ :Bi ³⁺	PDF # 54-0742	Cubic	–	–	–	0.238	(211)	[77]
Multicomponent borosilicates	450	490–550	CsPbBr ₃	JCPDS # 54-0752	Cubic	15.22	(100)	1.96	0.206	(220)	[78]
						21.64	(110)				
						26.52	(111)				
						30.68	(200)				
						37.78	(211)				
						43.90	(220)				
Zinc–borosilicates	400	500	CsPbBr ₃	JCPDS # 54-0752	Cubic	–	–	5.28	0.338	(111)	[79]

(Continued)

Table 2. (Continued).

Glass matrix/ composition	T_g [°C]	T_c [°C]	NCs	Referenced card	Crystal system	2 θ value [°]	Lattice plane	Size [nm]	d [nm]	Plane	Refs.
Borosilicates	350	475	CsPbBr ₃	PDF # 54-0742	Cubic	21.55 30.65 37.77 43.89	(110) (200) (211) (220)	—	0.238	(211)	[80]
Zinc-borosilicates			CsPbBr ₃	JCPDS # 54-0752	Cubic	—	—	30	0.352	(111)	[81]
Zinc-tellurites	450	480–600	CsPbBr ₃ :Eu ³⁺	JCPDS # 54-0752	Cubic	15.1 21.5 30.6 37.7 43.8	(100) (110) (200) (211) (220)	—	0.2332 — 0.3095 — 0.3273	(211) — (200) — (111)	[82]
Zinc-tellurites	230	250	CsPbBr ₃ :0.4mol%Ag ⁺ CsPbBr ₃ :0.5mol%Ag ⁺	PDF # 54-0742	Cubic	—	—	—	0.409 0.320	(110) (111)	[83]
Zinc-boro- aluminosilicates	400	480–540	CsPbBr ₃ CsPbBr ₃ :Eu ³⁺	JCPDS # 54-0752	Cubic	— 15.21 21.55	— (100) (110)	16.2 9.8	0.305 0.295	(200)	[84]
Zinc-calcium-boro- aluminosilicates	400	500	CsPbBr ₃ :Eu ³⁺ ,Tm ³⁺	PDF # 54-0742	Cubic	30.47 37.54 43.66	(200) (211) (220)	2.05– 4.40	—	—	[85]
Zinc-borosilicates	—	450	CsPbBr ₃	JCPDS # 54-0752	Cubic	15.16 21.54 30.62 37.80 43.80	(100) (110) (200) (211) (220)	4.0	0.337	(111)	[86]
Phosphates	150	—	CsPbBr ₃	JCPDS # 54-0752	Cubic	— 15.1 21.5	— (100) (110)	—	0.290 0.200	(200) (220)	[87]
Zinc-tellurites	250	280–310	CsPbBr ₃ :V ⁵⁺	PDF # 54-0742	Cubic	30.6 37.7 43.8	(200) (211) (220)	—	0.2098	(220)	[88]
Tellurites	270	340	CsPbBr ₃	PDF # 54-0742	Cubic	—	—	7–15	—	—	[89]
Zinc-calcium- boroaluminates	350	460/470	CsPbBr ₃	JCPDS # 75-0412	Cubic	—	—	15.2	0.239	(211)	[90]
—	—	—	GU-CsPbBr ₃	JCPDS # 75-0412	Cubic	—	—	9.8	0.404	(110)	This work
Zinc-strontium- boroaluminates	400	490	CsPbBr ₃ :1.1%Lu ³⁺ CsPbBr ₃ :1.1%La ³⁺ CsPbBr ₃	ICSD # 29073 ICSD # 29073	Cubic	— 24.48 30.51 37.73 43.68	— (110) (200) (211) (220)	4.3 3.8 —	0.346 0.409 —	(111) (110) —	This work
			CsPbBr ₃ :0.5%La ³⁺	ICSD # 29073	Cubic	21.55 30.51 37.78 43.71	(110) (200) (211) (220)	—	—	—	This work
			CsPbBr ₃ :0.5%Lu ³⁺	ICSD # 29073	Cubic	21.56 30.53 37.81 43.71	(110) (200) (211) (220)	—	—	—	This work

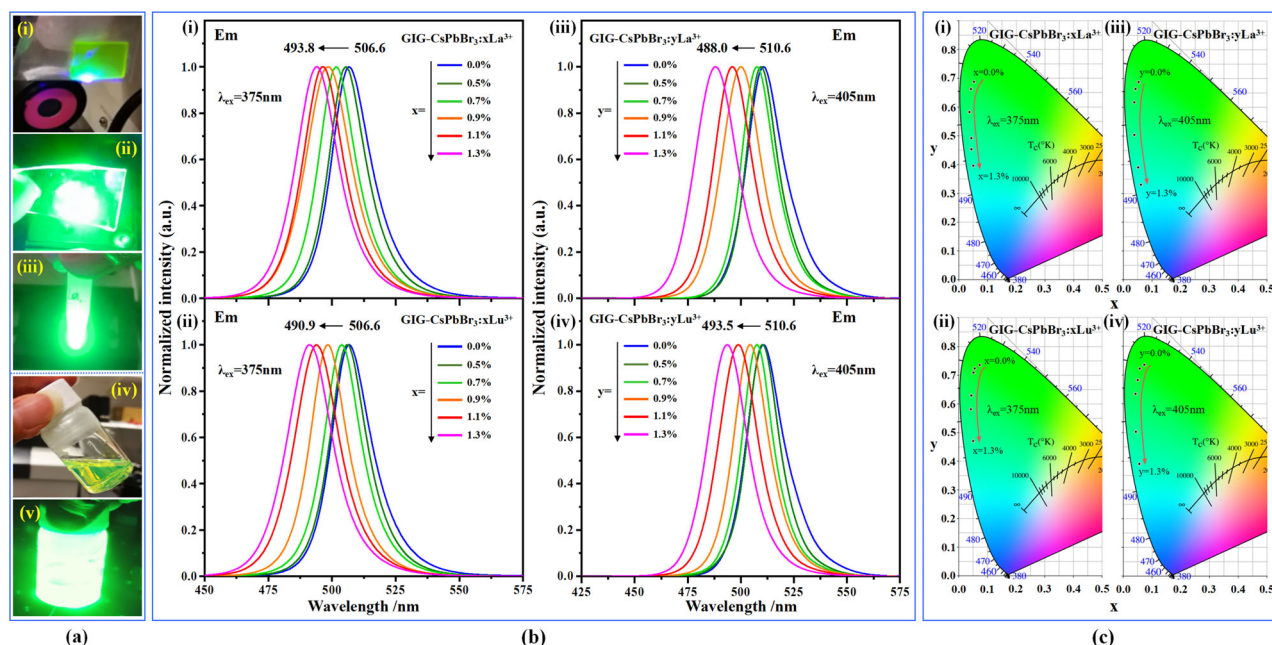


Figure 3. a) Digital photographs of GIG-CsPbBr₃ NCs recorded under a 405 nm laser in form of monolithic bulk glass (i), powders deposited on a quartz glass slide (ii), and immersed in the RT water (iii), along with that of acetone-suspended GU-CsPbBr₃ NCs upon exposure to the natural daylight (iv) and a 405 nm laser (v). b) Emission spectra of GIG-CsPbBr₃:xLa³⁺ and GIG-CsPbBr₃:yLu³⁺ ($x, y = 0; 0.5\% \leq x, y \leq 1.3\%$) NCs upon excitation with a 375 nm (i,ii) and with a 405 nm laser (iii,iv), where the two laser wavelengths have been labeled in each figure. c) The CIE chromaticity coordinates of GIG-CsPbBr₃:xLa³⁺ and GIG-CsPbBr₃:yLu³⁺ NCs, which are based on the emission spectra depicted in (b).

Table 3. Emission positions, FWHM values, and CIE chromaticity coordinates of GIG-CsPbBr₃:xLa³⁺ and GIG-CsPbBr₃:yLu³⁺ ($0 \leq x, y \leq 1.3\%$) NCs. These values are obtained and/or calculated on basis of the PL spectra of Figure 3b.

La/x	$\lambda_{\text{ex}} = 375 \text{ nm}$			$\lambda_{\text{ex}} = 405 \text{ nm}$		
	λ_{em} peak [nm]	FWHM [nm]	CIE values	λ_{em} peak [nm]	FWHM [nm]	CIE values
0	506.6	18.8	(0.0593, 0.6874)	510.9	20.9	(0.0736, 0.7355)
0.5%	505.5	17.3	(0.0427, 0.6630)	509.6	17.8	(0.0561, 0.7238)
0.7%	501.6	17.5	(0.0377, 0.5826)	507.6	18.7	(0.0518, 0.7089)
0.9%	498.2	20.9	(0.0443, 0.4917)	500.0	21.8	(0.0446, 0.6288)
1.1%	496.6	19.0	(0.0442, 0.4533)	495.9	21.1	(0.0425, 0.5812)
1.3%	493.8	19.7	(0.0508, 0.3965)	488.2	23.3	(0.0502, 0.4703)

Lu/y	$\lambda_{\text{ex}} = 375 \text{ nm}$			$\lambda_{\text{ex}} = 405 \text{ nm}$		
	λ_{em} peak [nm]	FWHM [nm]	CIE values	λ_{em} peak [nm]	FWHM [nm]	CIE values
0	506.6	18.8	(0.0593, 0.6874)	510.9	20.9	(0.0736, 0.7355)
0.5%	506.1	17.4	(0.0428, 0.6646)	510.3	17.8	(0.0571, 0.7233)
0.7%	503.8	17.2	(0.0393, 0.6172)	507.6	17.3	(0.0706, 0.6832)
0.9%	498.2	17.4	(0.0386, 0.5035)	504.3	19.6	(0.0433, 0.6342)
1.1%	493.8	20.6	(0.0522, 0.3904)	408.9	21.7	(0.0445, 0.5032)
1.3%	490.9	20.9	(0.0607, 0.3305)	493.5	21.9	(0.0560, 0.3901)

505.5 nm) and 405 nm (i.e., 509.6 nm) slightly differ respectively from that of 506.1 and 510.3 nm of the GIG-CsPbBr₃:0.5%Lu³⁺ NCs. We can learn that this PL difference is similar to the 2θ -reflection shift that is not very obvious at a low doping rate but becomes more and more obvious as the La³⁺ and Lu³⁺ contents are increased. This, to some extent, also reflects the slight variation of CsPbBr₃ cell lattice caused by the La³⁺ and Lu³⁺ ions.

We correlate the PL shifts to the CsPbBr₃ lattice cell modification caused by the substitution of larger Pb²⁺ lattice ions by smaller La³⁺ or Lu³⁺ doping ions. All corresponding values of PL peak positions, full width at half maximum, and CIE chromaticity coordinates are presented in Table 3 and Figure 3c.

A step further, we also plotted the peak shifts (hereafter, $\Delta(\lambda_{\text{exc}})$ expressed in cm⁻¹) against the Ln³⁺ doping rates to illustrate the

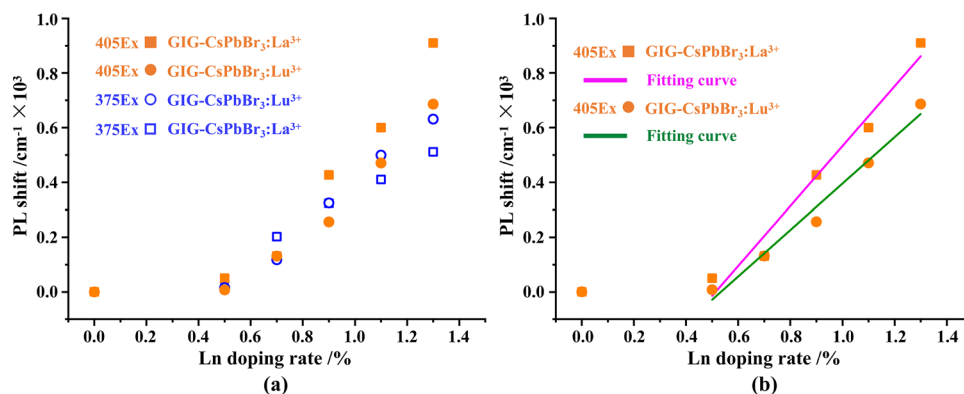


Figure 4. a) PL shift in cm^{-1} against the x or y values (i.e., the rates of La^{3+} or Lu^{3+} doping) in the $\text{GIG-CsPbBr}_3:\text{La}^{3+}$ and $\text{GIG-CsPbBr}_3:\text{Lu}^{3+}$ NCs. b) Linear fitting of PL shift in cm^{-1} against the x or y values in the $\text{GIG-CsPbBr}_3:\text{La}^{3+}$ (orange-yellow curve) and $\text{GIG-CsPbBr}_3:\text{Lu}^{3+}$ NCs (green curve) upon excitation at a 405 nm laser.

observed PL change. This PL shift, as shown in Figure 4a, is linear for x or y exceeding the threshold value of 0.5%, and it follows: 1) $\Delta(375 \text{ nm}, \text{La}^{3+}) = 19740 + 567x$, and $\Delta(375 \text{ nm}, \text{Lu}^{3+}) = 19740 + 806y$ for 375 nm excitation; 2) $\Delta(405 \text{ nm}, \text{La}^{3+}) = 19573 + 1095x$, and $\Delta(405 \text{ nm}, \text{Lu}^{3+}) = 19573 + 848y$ for 405 nm excitation (Figure 4b). The two linear equations indicate that the spectral shifts are more pronounced upon excitation with 405 nm than 375 nm laser light or by La^{3+} doping than Lu^{3+} doping under 405 nm excitation, as evidenced by the gradual rise of the gap between the two linear fitting curves in Figure 4b. This is the reason why we collected all forthcoming PL experiments upon 405 nm rather than by 375 nm excitation.

To theoretically support our interpretation of the origin of the above spectral tuning, we have calculated further the electronic structure of Ln^{3+} -free ($\text{Ln} = \text{La}, \text{Lu}$) and -doped CsPbBr_3 in the approximation of a homogeneous replacement of the six-fold coordinated Pb atoms by the La or Lu atoms (see Figure 5). Given the ionic radii and charge difference between Pb^{2+} (1.19 Å), La^{3+} (1.1032 Å), and Lu^{3+} (0.861 Å) ions at six Br^- -coordination numbers, we have carried out the calculations without and with Br^- -related vacancies. Detailed structural patterns and information rebuilt based upon the DFT-optimized lattice parameters (Table 1) are shown in Figure 5a. In undoped CsPbBr_3 , each Pb atom is surrounded by six Br atoms, with a distance of 2.99 Å for the Pb–Br bond. When Pb atoms are replaced by, for instance, the La atoms, the distance of the La–Br bond is decreased to 2.92 Å, which is shorter than that for the Pb–Br bond. When a Br^- -related vacancy is positioned adjacently to La, then the La–Br bond is changed to 2.96 Å. This illustrates that the CsPbBr_3 lattice is affected locally by doping with Ln^{3+} ions and further by considering Br^- -related-anionic vacancies. Figure 5b shows the band structure of the CsPbBr_3 calculated at the GGA level. The direct bandgap energy at point R amounts 1.75 eV, which agrees with previous theoretical reports on this perovskite.^[91,92] The spin-orbit coupling (SOC) strength of Pb^{2+} and Br^- ions may change the bandgap of CsPbBr_3 (0.6 eV, GGA + SOC), but our objective is to capture the trend of bandgap energies where the SOC is not expected to affect this trend a lot.^[93] Thus, the rest of the optical bandgap evaluation in the Ln^{3+} -doped CsPbBr_3 was performed by using the GGA method. With this approximation, we present in Figure 5c partial density of states (PDOS) of CsPbBr_3 with dif-

ferent amounts of La atoms inserted into Pb sites. The results depicted in Figure 5c(i–iii) reveal an increase of the bandgap from 1.75 to 2.33 eV as the x value is raised from 0 to 0.06, and a sudden decrease to 2.27 eV when the x value goes further to 0.08. That is, the behavior of the last point in the bandgap, as the red curve shows, is abnormal since this value is smaller than that of the second-to-last point. This is inconsistent with our expectations that the bandgap should continuously increase with the increase of the Ln^{3+} doping rate. In this case, the Br^- -related vacancies were then considered in the calculation, and the corresponding bandgap energies are shown in Figure 5c(iv–vi). After comparison, it is clear that when taking into account the Br^- -related defects (Figure 5d (blue curve)), the bandgap energy values at each La^{3+} doping rate are all smaller than that of the Br^- -vacancies-free counterparts. The results are reasonable since doping the external ions into a crystal matrix sometimes involves the generation of vacancies that can reduce the total energy.^[94,95] Thus, the $\text{CsPb}_{1-x}\text{La}_x\text{Br}_{3-z}$ as the x value increases from 0.02 to 0.08 feature an increase in bandgap energies from 1.53 to 1.83 eV. It is inconsistent with the trend of bandgap change in Figure 5d (curve 1) but “rectifies” the second-to-last point, thereby showing the consistency of the bandgap change trend with the PL position shift trend in Figure 3b. Although carried out with x values significantly larger than the experimental ones, the DFT calculations reveal that the bandgap of CsPbBr_3 tends to increase as the Pb^{2+} cations are replaced by trivalent La^{3+} cations. Assuming that the excitonic character of the CsPbBr_3 absorption or emission band results from the recombination of electron and holes pairs that are produced after bandgap excitation, a rise of bandgap energies in the CsPbBr_3 after being doped with the Ln^{3+} ions can thus be assigned to the shrinkage of the CsPbBr_3 lattice that results from the Ln^{3+} -doping and the creation of Br^- -related vacancies, which then mostly accounts for the PL positions’ shift as Figure 3 exhibits.

4.3. Stabilities under External Exposures

Four kinds of experimental tests were designed to qualify the stabilities of the obtained samples under external exposures. For this, three batches of fine GIG-powders were selected. All the PL

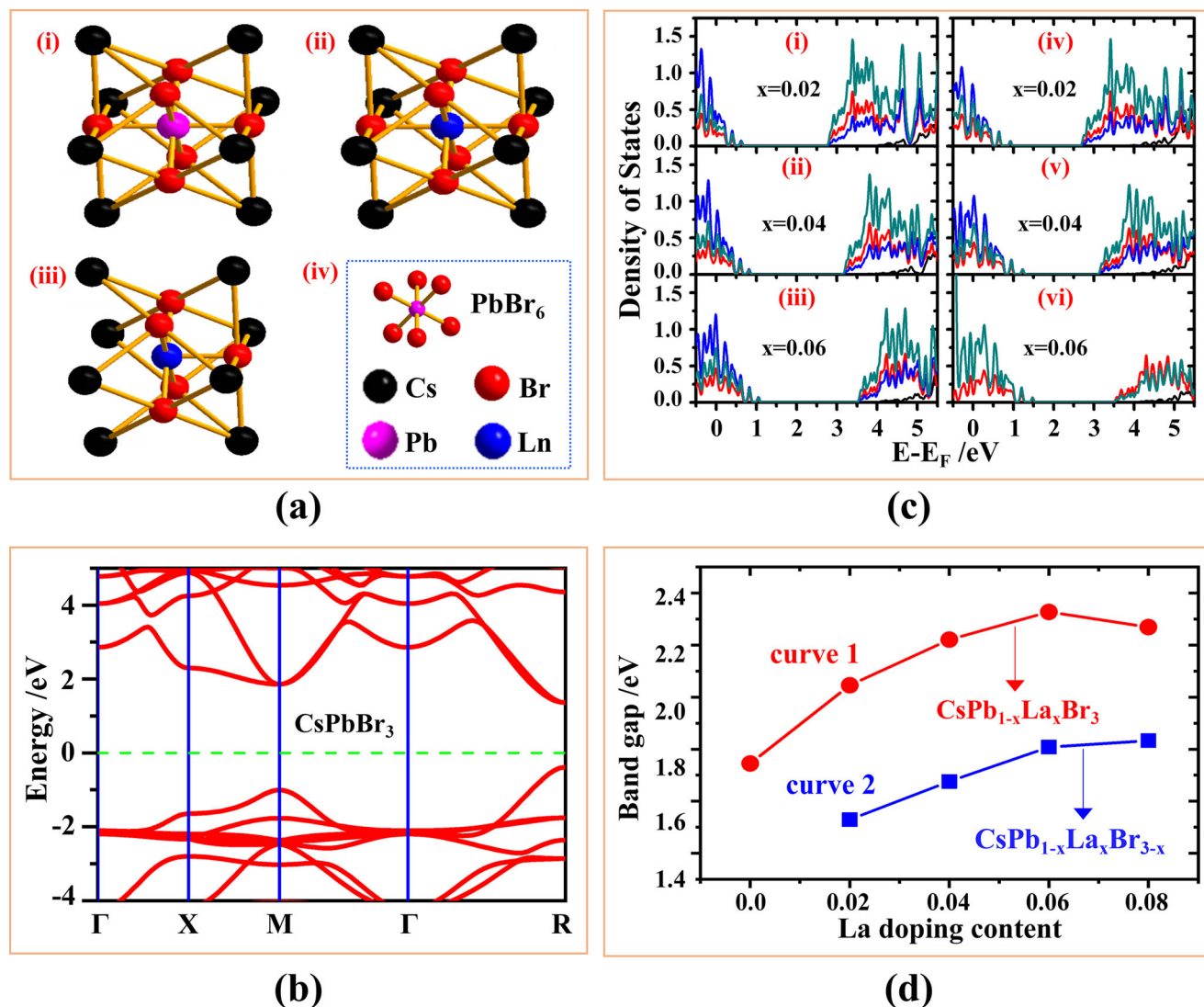


Figure 5. a) Detailed structural information of CsPbBr₃ (i), replacement of Pb site by Ln atom without (ii) and with (iii) consideration of Br[−]-related vacancies, in which the Cs, Br, Pb, and Ln atoms, marked respectively in black, red, purple, and blue, are shown in (iv). b) DFT-calculated band structure of CsPbBr₃. c) Density of states (DOS) by replacement of Pb sites with La atoms in the CsPbBr₃ without (i–iii) and with (iv–vi) consideration of Br[−]-related vacancies. d) Dependence of bandgap energies on the La doping rates without (red line) and with (blue line) consideration of Br[−]-related vacancies. Note that the number of the Br vacancies (i.e., *z*) in (d) is an independent value, which should be not as much as the La atoms (i.e., *x*).

experiments were collected upon excitation at 405 nm, a wavelength for which the spectral shifts with the increase of the Ln³⁺ doping rates, as we mentioned above, is experienced to be larger than upon 375 nm excitation.

4.3.1. Effect of Moisture

Figure 6 shows the normalized PL (NPL) spectra of GIG-CsPbBr₃ and GIG-CsPbBr₃:0.5%Ln³⁺ (Ln = La, Lu) powder samples that were tested versus moisture following three procedures: (a) an immersion in water at RT for up to 300 days, (b) an immersion in temperature-increasing water until it boils, and (c) in boiling water for up to 48 h. For each series of tests, the alteration of the powder GIG-samples was evaluated by collecting the emission

spectra, making sure that all measurement parameters were kept identical. The NPL intensity (NPLI) was evaluated as the area integrated in the spectral range of 475–575 nm, normalizing to the maximum PL intensity. Table 4 and Figure 7 show the variation of NPLI and emission maxima against the immersion time or temperature.

With the increase of an immersion time in water at RT, no significant change of positions and spectral shape (Figure 6a(i–iii)) is observed in the three GIG-samples. For GU-CsPbBr₃ NCs, a pronounced depreciation of the luminescence is observed (Figure 6a(iv)), where >58% and >99% of the initial PL intensity are lost after 24 and 300 days immersion (Figure 7a (purple curve)), respectively. By contrast, the three GIG-samples preserve >90%, >84%, and >67% of the initial intensity (*t* = 0) at an immersion time of 8 (red), 48 (blue), and 300 days (yellow) (Figure 7a),

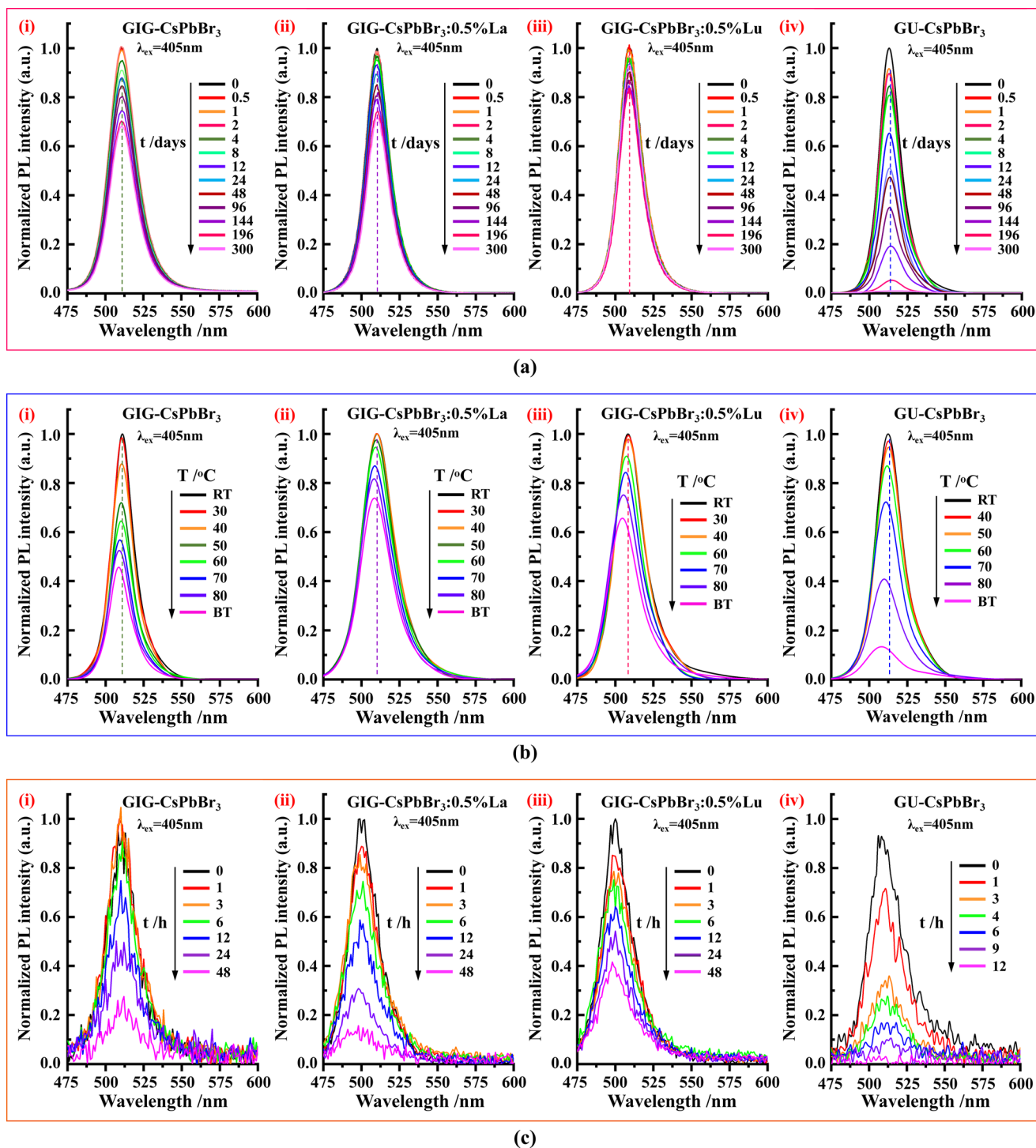


Figure 6. Normalized PL spectra ($\lambda_{\text{ex}} = 405 \text{ nm}$) of GIG-CsPbBr₃ (i), GIG-CsPbBr₃:0.5%La³⁺ (ii), and CsPbBr₃:0.5%Lu³⁺ (iii), and GU-CsPbBr₃ (iv) NCs recorded: a) after continuous immersion in the RT water for 300 days; b) with heating the water until it boils, note here that the total duration of increasing the water from RT to boiling temperature (BT) is $\approx 15 \text{ min}$; and c) kept in the boiling water for 48 and 12 h, respectively. RT, BT, t , and T denote room temperature, boiling temperature, immersion time, and temperature, respectively. The La³⁺ and Lu³⁺ doping rates have also been given in the figures.

Table 4. Dependence of normalized PL intensity (NPLI) and peak position on immersion time in room temperature (RT), increasing temperature (IT), and boiling temperature (BT) water in the GIG-CsPbBr₃, GIG-CsPbBr₃:Ln³⁺ (Ln = La, Lu), and GU-CsPbBr₃ NCs. All the data are from the PL spectra of Figure 6.

RT [d]	GIG-CsPbBr ₃		GIG-CsPbBr ₃ :0.5%La ³⁺		GIG-CsPbBr ₃ :0.5%Lu ³⁺		GU-CsPbBr ₃	
	NPLI	Peak [nm]	NPLI	Peak [nm]	NPLI	Peak [nm]	NPLI	Peak [nm]
0	1	510.8	1	510.4	1	509.1	1	512.4
0.5	0.998	511.1	0.983	510.1	0.987	509.1	0.917	512.8
1	0.997	511.5	0.979	510.4	0.978	509.1	0.916	512.8
2	0.986	511.1	0.980	510.1	0.950	509.1	0.898	512.8
4	0.946	511.1	0.970	510.4	0.943	509.4	0.847	513.2
8	0.905	510.7	0.952	510.4	0.945	509.1	0.810	513.2
12	0.874	510.8	0.935	510.1	0.919	510.1	0.654	513.2
24	0.868	511.2	0.896	509.4	0.914	509.1	0.511	513.2
48	0.842	510.4	0.855	510.1	0.892	509.4	0.474	513.2
96	0.800	511.5	0.822	510.8	0.857	509.7	0.345	514.5
144	0.742	511.1	0.795	510.4	0.828	510.1	0.192	514.5
196	0.699	510.8	0.746	510.7	0.825	510.1	0.053	514.6
300	0.679	510.8	0.717	510.4	0.797	509.4	0.001	514.9

IT [°C]	GIG-CsPbBr ₃		GIG-CsPbBr ₃ :0.5%La ³⁺		GIG-CsPbBr ₃ :0.5%Lu ³⁺		GU-CsPbBr ₃	
	NPLI	Peak [nm]	NPLI	Peak [nm]	NPLI	Peak [nm]	NPLI	Peak [nm]
25 [RT]	1	510.8	1	510.4	1	508.4	1	511.8
30	0.986	510.8	0.999	510.1	0.994	508.4	–	–
40	0.877	510.2	0.995	510.1	0.979	508.4	0.961	511.4
50	0.720	510.6	0.975	509.8	–	–	0.934	511.4
60	0.645	510.5	0.946	509.4	0.909	507.3	0.864	511.4
70	0.568	509.7	0.870	508.7	0.843	506.6	0.723	511.1
80	0.524	509.3	0.817	508.4	0.751	505.3	0.408	509.7
BT	0.456	508.8	0.738	508.4	0.656	504.6	0.134	508.4

BT [h]	GIG-CsPbBr ₃		GIG-CsPbBr ₃ :0.9%La ³⁺		GIG-CsPbBr ₃ :0.9%Lu ³⁺		GU-CsPbBr ₃	
	NPLI	Peak [nm]	NPLI	Peak [nm]	NPLI	Peak [nm]	NPLI	Peak [nm]
0	1	509.9	1	499.7	1	499.8	1	509.3
1	0.994	509.8	0.885	500.2	0.852	499.1	0.766	510.2
3	0.965	508.9	0.838	499.5	0.784	499.8	0.385	512.1
4	–	–	–	–	–	–	0.297	511.6
6	0.952	510.5	0.744	500.3	0.749	499.4	0.181	511.3
9	–	–	–	–	–	–	0.109	512.4
12	0.786	509.9	0.586	499.9	0.639	500.2	–	–
24	0.486	509.9	0.312	498.5	0.539	499.6	–	–
48	0.273	510.1	0.155	498.9	0.412	498.5	–	–

respectively. All the four samples, as depicted in Figure 6b, show a blueshift (≈ 2 – 5 nm) of their emission position and a progressive depreciation of the luminescence with increasing the water temperature (Figure 7b). This is analogous to other luminescent materials exposed to an external temperature-increasing environment.^[39–41] This luminescence depreciation, however, is very obvious in GU-CsPbBr₃ NCs as the temperature is increased, and $\approx 87\%$ of the initial PL intensity is lost when the water boils. By contrast, the GIG-samples are much less affected by temperature, especially those doped with the La³⁺ or Lu³⁺ ions. They maintain $>74\%$ and $>58\%$ of the initial PL intensity recorded at the water starts boiling when continued to be placed

in the boiling water for 6 and 12 h (Figure 6c(i–iii), and Figure 7c). Comparatively, GU-CsPbBr₃ NCs, exposed to the same treatment, show a rapid PL intensity decrease (Figure 6c(iv), and Figure 7c) where $>61\%$ of the initial PL intensity is lost after only 3 h and almost 100% is lost after 12 h.

4.3.2. Corrosive Media

The PL depreciation was also analyzed by immersing the GIG-CsPbBr₃, GIG-CsPbBr₃:0.9%Ln³⁺ (Ln = La, Lu), and GU-CsPbBr₃ NCs in corrosive aqueous solutions with pH ranging

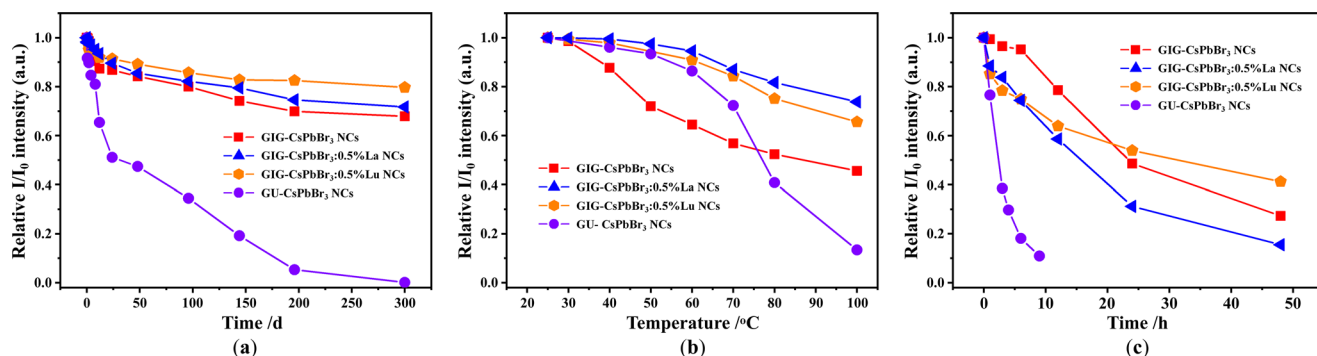


Figure 7. Variation of the normalized PL intensity of GIG-CsPbBr₃ (red), GIG-CsPbBr₃:0.5%La³⁺ (blue), CsPbBr₃:0.5%Lu³⁺ (yellow), and GU-CsPbBr₃ NCs (purple) against the immersion time in water at a) RT, b) temperature-increasing water, and c) boiling water.

from 1 to 14. Relevant treatments were maintained at room temperature for up to 56 h. Again, the NPL spectra and NPLI were used to illustrate the stabilities of these samples, and the results are shown in **Figure 8**. All the samples immersed in a specific pH value show a gradual decrease of the PL intensity with increasing immersion time (see Figure 8a, and the red (pH = 5) and blue (pH = 12) curves in Figure 8b–d). The bar plots in Figure 8b–d demonstrate the PL intensity decrease for all these samples exposed either to acidic or to basic environments after 12 h of immersion, but the GU-CsPbBr₃ NCs suffer much more PL depreciation in the same corrosive conditions, with reduction of the intensity exceeding 80% in pH below 5 or above 11 (bar plots in Figure 8e). The immersion time $t_{0.5}$, at which the GU-CsPbBr₃ NCs have lost 50% of their initial PL intensity, amounts ≈ 12 h at pH = 5 and ≈ 18 h at pH = 12 (Figure 8e). There is no significant change in the PL positions in the GU-CsPbBr₃ NCs (Figure 8a(iv)), but the PL intensity retains only $\approx 2\%$ of the initial PL intensity treated either at pH = 12 after 38 h of immersion or at pH = 5 for 30 h. The PL quenching is almost complete after 32 h of immersion in an acid solution (red curve) and 40 h in an alkali one (blue curve), as depicted in Figure 8e. By comparison, the PL depreciation of the GIG-samples after 12 h of immersion (see Figure 8b–d) is less than 20% for pH values over the range of 4–12, and less than 50% for staying even in, e.g., a strong acid and alkali solution with pH values of 1 and 14. These above results demonstrate the benefit of the glass matrix protection in sustaining the PL properties of CsPbBr₃ NCs under corrosive acid–base solution exposures, although we have also noticed that this shielding is more efficient under strong bases than that under strong acids. The $t_{0.5}$ values, associated with an acid solution with a pH value of 5, amount ≈ 56 , ≈ 30 , and ≈ 50 h in the GIG-CsPbBr₃, GIG-CsPbBr₃:0.9%La³⁺, and GIG-CsPbBr₃:0.9%Lu³⁺ NCs (Figure 8b–d, red curves), respectively.

4.3.3. Heating (+150 °C)–Cooling (–150 °C) Cycles

The GIG-CsPbBr₃, GIG-CsPbBr₃:0.7%Lu³⁺, GIG-CsPbBr₃:1.3%La³⁺, and GU-CsPbBr₃ NCs were selected to study the tolerance of PL stability against repeated heating–cooling cycles. The PL spectra were in situ measured by using the PL setup depicted in Figure 1b. To avoid the possible influence of defects-trapped carriers on the PL properties, all the four samples were

first rapidly heated for one cycle in the dark from –190 °C to +200 °C prior to any PL measurement, and then the PL spectra were recorded repeatedly in the sequence of –150 °C \leftrightarrow –70 °C \leftrightarrow 25 °C \leftrightarrow 70 °C \leftrightarrow 150 °C for up to 30 cycles. Obviously, these temperatures are all much lower than the glass transition temperature (i.e., 400 °C) or the crystallization temperature (i.e., 490 °C), meaning the repeated heating–cooling experiments would not cause the phase transition of CsPbBr₃ NCs grown in the glass matrix. Meanwhile, Yang et al.^[96] reported the temperature-dependent XRD patterns of the Eu³⁺-doped CsPbBr₃ glass ceramic, and found that all the major 2 θ -reflection peaks as the temperature even arrives to 380 °C shift slightly to lower diffraction angle but their positions agree well with that of JCPDS # 54–0752, without the disappearance of the major 2 θ -reflection peaks or the appearance of new observable diffraction peaks unique for other phases like the orthorhombic phase as mentioned by Malyskhin et al.^[97] These results indicate that the phase change is highly unlikely according to our current XRD patterns recorded at room temperature. As shown in **Figure 9a–d(i)**, a thermal PL quenching appears in these samples as the temperature increases. Apart from an earlier stage in the heating–cooling cycles, the PL intensity of the three GIG-samples is almost completely restored and varies little with further repeated heating–cooling experiments (Figure 9a–c(iii)). Additionally, no significant change of PL positions is observed at each given temperature (Figure 9a–c(ii)), and the GIG samples, exposed to 30 heating–cooling cycles, are able to keep >70% of their respective PL intensity initially recorded at –150, –70, 25, 70, and 150 °C. Typically, the GIG-CsPbBr₃:0.7%Lu³⁺ saves 90% of the initial PL intensity initially measured at –150 °C or at 70 °C after 30 heating (+150 °C) \leftrightarrow cooling (–150 °C) cycles. By contrast, however, the GU-CsPbBr₃ NCs experience a fast depreciation of their PL intensity as the temperature is raised (Figure 9d(i)), with a temperature corresponding to a loss of 50% of the low temperature intensity $T_{0.5} \approx -50$ °C. The PL signals at +110 °C are very weak, only keeping $\approx 0.35\%$ of the PL intensity initially recorded at –190 °C (Figure 9d(iii)), revealing that the PL quenching of the GU-CsPbBr₃ NCs is almost complete at 110 °C. This luminescence depreciation, which perhaps comes from a thermal dissociation of the self-trapped excitons (STEs), is concomitant with a thermal-driven shift of the emission positions from 519.1 to 512.3 nm (Figure 9d(i)), although these PL positions at a fixed temperature do not vary significantly as the

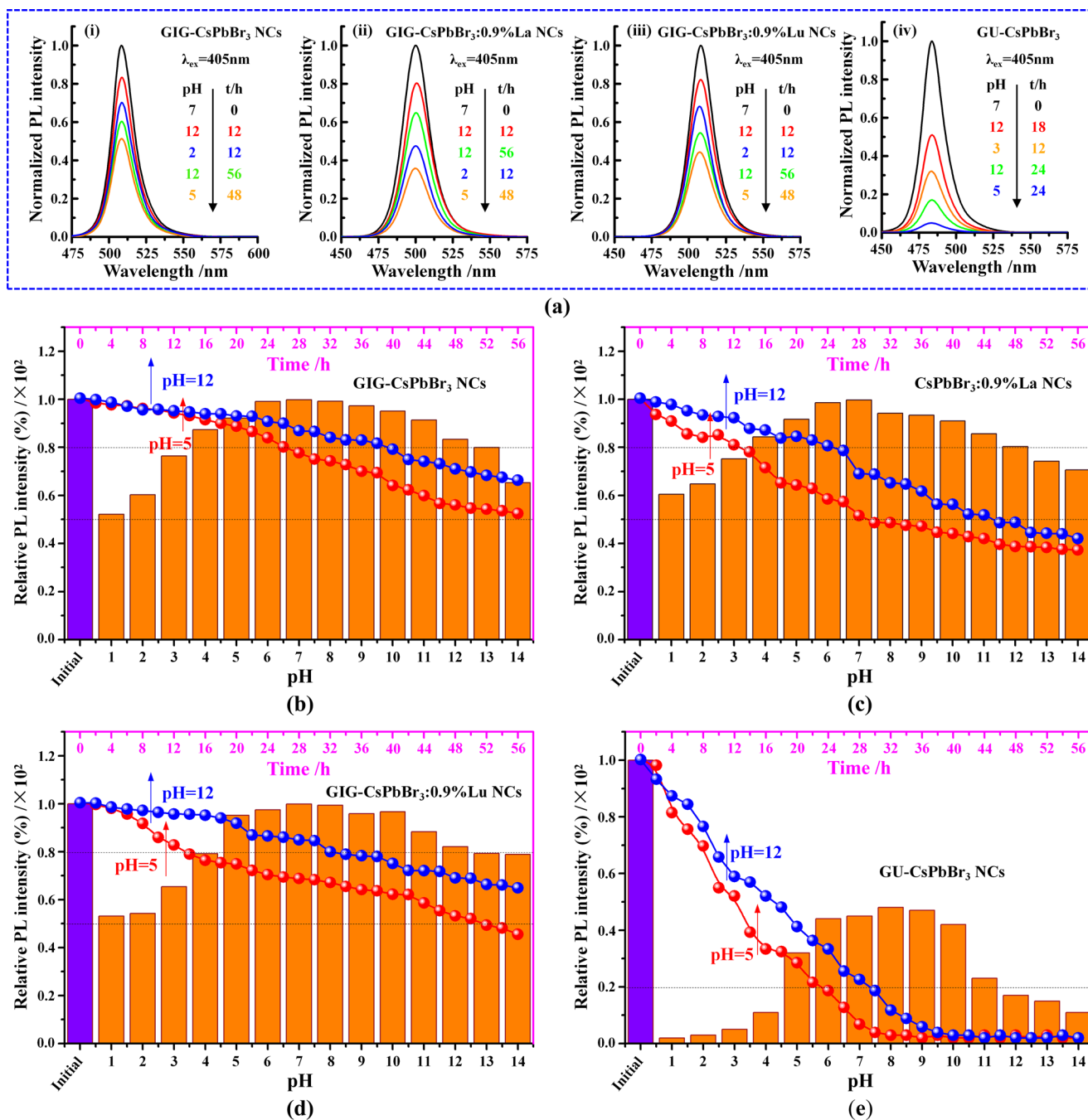


Figure 8. a) Normalized PL spectra of GIG-CsPbBr₃ NCs (i), GIG-CsPbBr₃:0.9%La³⁺ (ii) and GIG-CsPbBr₃:0.9%Lu³⁺ (iii) NCs, and GU-CsPbBr₃ (iv) NCs stayed in an acid and alkali solution with different pH values for different immersion duration. b–e) Dependence of the PL intensity of GIG-CsPbBr₃ NCs (b), GIG-CsPbBr₃:0.9%La³⁺ (c) and GIG-CsPbBr₃:0.9%Lu³⁺ (d) NCs, and GU-CsPbBr₃ (e) NCs on the pH values over the range of 1–14 (histogram) for an immersion time of 12 h, as well as dependence of the relative PL intensity on the immersion time in a pH = 5 acid solution (red curve) and in a pH = 12 alkali solution (blue curve).

heating–cooling cycles are increased (Figure 9d(ii)). Unlike the GIG-samples, cooling down to -150°C cannot restore the initial PL intensity in the GU-CsPbBr₃ NCs, indicating unrecoverable PL depreciation. It sustains only $\approx 52\%$ and $\approx 78\%$ of the initial PL intensity after 4 and 8 cycles of the cooling (-150°C) \leftrightarrow heating ($+150^\circ\text{C}$) experiments, as seen in Figure 9d(iii).

4.3.4. Laser Light Irradiation

Local heat generated by a focused laser beam can reach up to 150°C or more,^[31,98,99] causing severe PL quenching either by stimulating the aggregation of NCs and/or by local thermal effect. Such PL quenching can either be reversible, for instance,

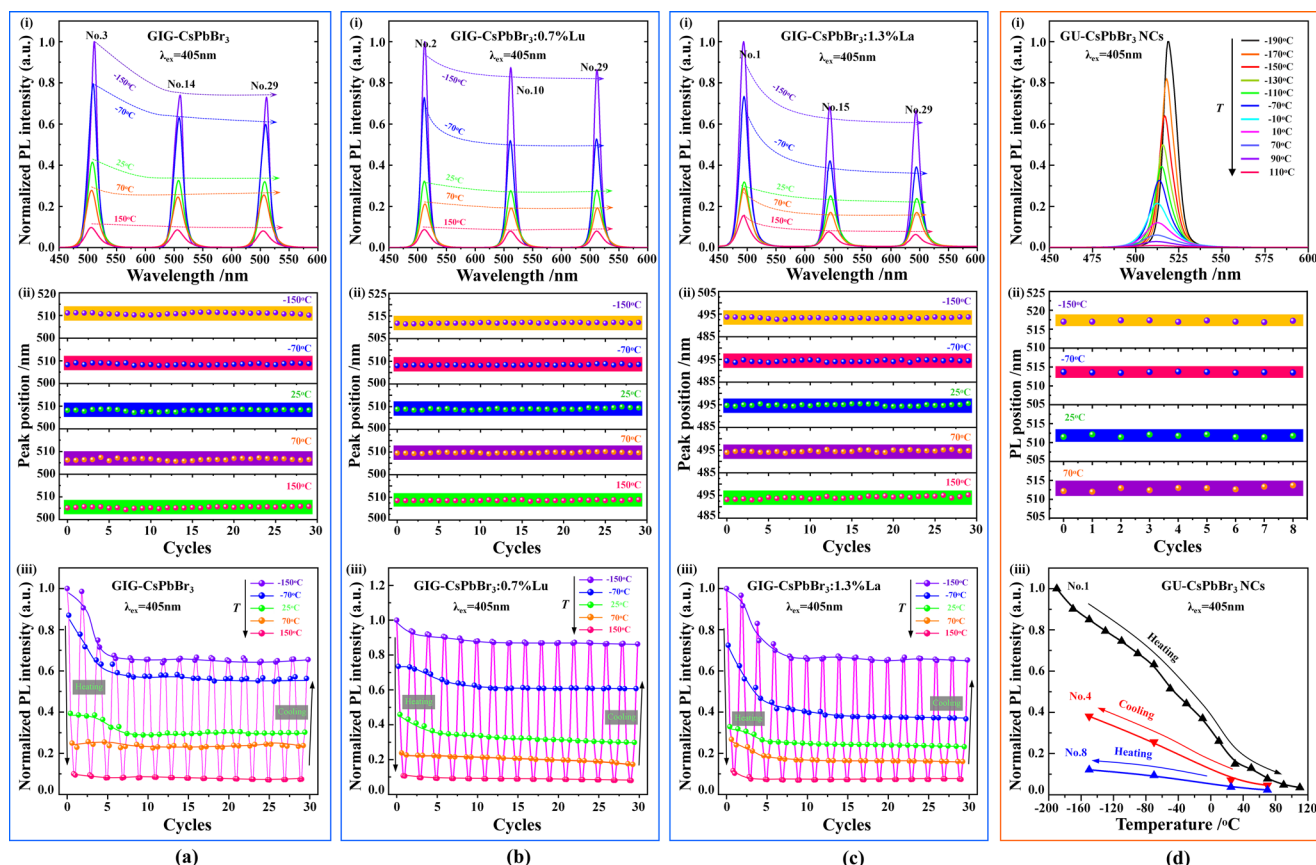


Figure 9. a–c) Normalized PL spectra (i) of GIG-CsPbBr₃ (a), GIG-CsPbBr₃:0.7%Lu³⁺ (b), and GIG-CsPbBr₃:1.3%La³⁺ (c) NCs recorded at the temperature points of −150, −70, 25, 70, and 150 °C, along with dependence of PL positions (ii) and intensity (iii) on 30 cycles of the heating–cooling experiments. d) Normalized PL spectra (i) of GU-CsPbBr₃ NCs recorded in a temperature range of −190 ↔ +110 °C, and dependence of PL positions (ii) and intensity (iii) on the heating–cooling experiments. Note that the number of heating–cooling cycles, for instance in the PL spectra, has been labeled beside each curve. *T* denotes temperature in the unit of °C. All the PL spectra of the samples are recorded upon exposure to a 405 nm laser.

in the case of thermal dissociation of the STEs or quenching by cross-over to the ground state, or be irreversible in case of unrecoverable damage resulting from photobleaching or permanent change of the micro/nanostructure or crystal phase. It is therefore important for us to evaluate the PL quenching when taking into consideration the potential application of the GIG-samples in the laser-converted lighting technology. The PL results of GIG-CsPbBr₃, GIG-CsPbBr₃:1.1%La³⁺, GIG-CsPbBr₃:1.1%Lu³⁺, and GU-CsPbBr₃ NCs samples under a 405 nm laser irradiation are presented in Figure 10. As can be seen, laser–matter interaction is deleterious in all four samples for a long term of laser light irradiation, although they show different PL intensity variations as the irradiation time increases. The GIG-CsPbBr₃ (Figure 10a) and GU-CsPbBr₃ NCs (Figure 10d) show a luminescence depreciation as the irradiation time is increased. All the GIG-samples do not reach the *t*_{0.5} time after exposure to the laser beam for 72 h or more (Figure 10a–c), but the *t*_{0.5} of GU-CsPbBr₃ NCs amounts only ≈10 h (Figure 10d). The GU-CsPbBr₃ NCs experience ≈82% of PL depreciation after ≈78 h and, with the increase of time, show a PL intensity decrease much faster than the GIG-samples. Meanwhile, the flat change in the irradiation-free interval of 80.4–121.6 h reveals that the PL intensity cannot be restored when the continuous laser irradiation is stopped (blue points

in Figure 10d). This indicates a permanent and irreversible PL degradation of properties in GU-CsPbBr₃ NCs. By comparison, the luminescence depreciation of GIG-CsPbBr₃ (Figure 10a) and GIG-CsPbBr₃:1.1%Ln³⁺ (Ln = La, and Lu, Figure 10b,c) samples amounts respectively 31.3%, ≈24.9%, and 19.5% after 72, 78, and 80.5 h of laser irradiation. In contrast to GU-CsPbBr₃ NCs, the PL loss from these GIG samples can be restored partially when the continuous irradiation is stopped (blue points in Figure 10a–c), meaning that the CsPbBr₃ NCs, at least for a part of them, protect from irreversible damage on the PL properties. The PL intensity shows a very slow self-recoverable process in the dark that we ascribe to a progressive heat dissipation within the samples, but can be accelerated with the assistance of an artificial halogen lamp operated at full spectrum. For instance, the GIG-CsPbBr₃:1.1%La³⁺ NCs recover ≈59% of the lost PL intensity when exposed to the halogen lamp for 10 min and basically reach ≈100% after 9 h of exposition (purple points in Figure 10b). Besides, an initial rise of 20–25% of PL intensity during the 1–2.5 h stage of a 405 nm laser light irradiation followed by a subsequent intensity decrease with a further prolongation of laser irradiation is observed in the Ln³⁺-doped GIG-systems (Figure 10b,c), but does not appear in GIG-CsPbBr₃ and GU-CsPbBr₃ NCs that the PL quenching starts immediately once the laser is on.

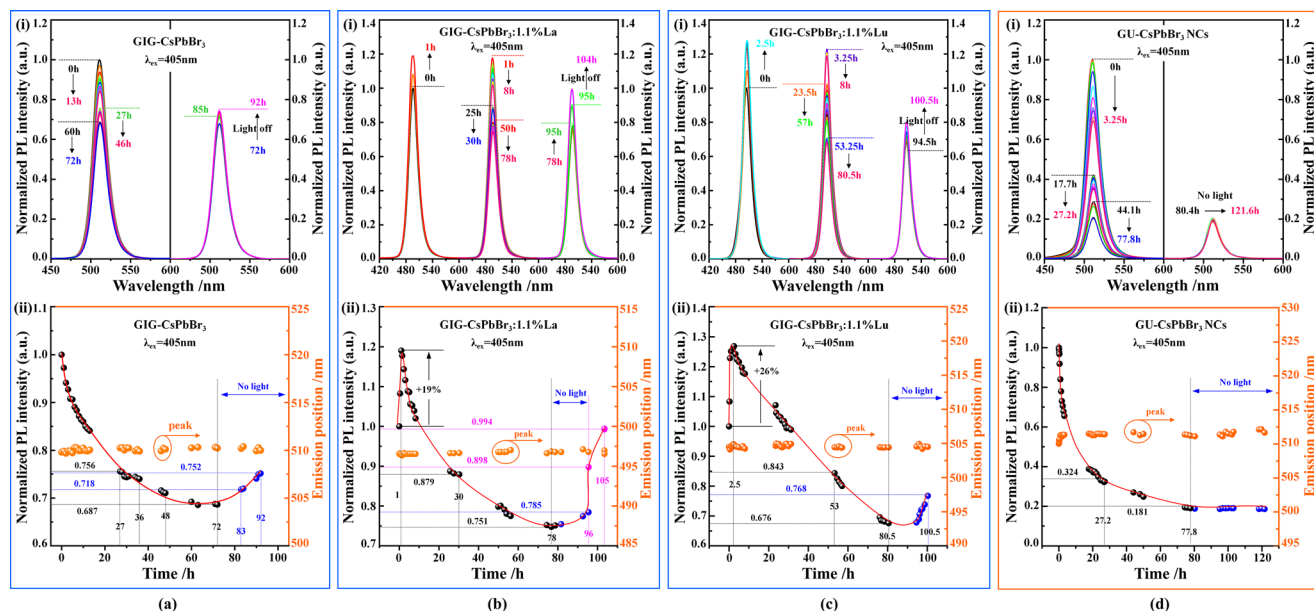


Figure 10. (i) Normalized PL spectra ($\lambda_{\text{ex}} = 405 \text{ nm}$) of a) GIG-CsPbBr₃, b) GIG-CsPbBr₃:1.1%La³⁺, and c) GIG-CsPbBr₃:1.1%Lu³⁺ as well as d) GU-CsPbBr₃ NCs upon exposure to a 405 nm laser irradiation for 72, 78, 80.5, and 77.8 h, respectively. (ii) Dependence of the relative PL intensity on the irradiation time (black dots) and after laser-switching-off time (blue dots). Additionally, the typical PL spectra of the four samples, which were recorded after switching off the laser light and then kept respectively in the dark for 20 h (i.e., 72 → 92 h), 26 h (i.e., 78 → 104 h), 6 h (i.e., 94.5 → 100.5 h), and 41.2 h (i.e., 80.4 → 121.6 h), are shown in (i). Meanwhile, dependence of the relative PL intensity on the irradiation time of an artificial halogen lamp in the typical GIG-CsPbBr₃:1.1%La³⁺ sample is also shown, as the yellow dots depicted in Figure 11b(ii).

4.4. Discussion and Analysis on the Observed PL Properties

The luminescence of PM nanocrystals results from electron transitions between the valence band (VB) and the conduction band (CB) with subsequent formation of the STEs that emit when the electron-hole pairs recombine. The VB top of ABX₃-typed MHPs typically consists of an antibonding state that forms between metal s and halide p orbitals, whereas the CB bottom is a mixing of metal p and halide p orbitals with prominent nonbonding character. As a result, any change of the metal-halide bonding affects the energy of the VB top without affecting much the CB bottom. Particularly, a larger orbital overlap induced by, for instance, the chemical substitution, lattice distortion, and external pressure, will destabilize the VB top, reduce the bandgap and lead to a red-shift of the photoluminescence. It occurs for instance in the case of tilting of the octahedral BX₆ units that take place across the cubic-to-orthorhombic phase transition.^[97,100] Cheetham and co-workers^[101] and Michael and co-workers^[102] reported that the VB top of the CsPbBr₃ features an antibonding Pb6s²-Br2p⁶ character while the CB bottom has a nonbonding Pb6s²-Br2p⁶ character in such a way that the optical transition is sensitive to the octahedral tilting of the PbBr₆ units. It is a unique character particularly suitable for probing optically the degree of tilting. As previously described in Section 4.2, the increase of Ln³⁺ doping levels is concomitant with a blueshift of the PL positions (Figure 3b). We ascribe it to a less tilted crystal structure and conclude that the structure of Ln³⁺ doped and undoped CsPbBr₃ NCs in the borosilicate-based glass as the Ln³⁺ content is raised is closer to a cubic phase, probably due to a thermal-assisted re-ordering of the CsPbBr₃ NCs toward a more perfect cubic phase. In this sense, tilting together with the relevant PL shift will not

be so obvious in the GIG-samples (Figure 9a–c(i)) as compared to the GU-CsPbBr₃ NCs (Figure 9d(i)). Therefore, the luminescence spectroscopy offers a much more sensitive tool than the X-ray diffraction to probe the effect of dopants at low doping rates.

Coming back to the DFT calculation, a continuous rise of bandgap energies with the increase of, e.g., the La³⁺ doping rates, appears in the CsPbBr₃ when taking into account Br⁻-related vacancies. Based on the thermoluminescence (TL) (i.e., a type of luminescence that can be used for reflecting the traps' status in form of temperature-dependent luminescence) measurements, Zhang et al.^[34] reported a TL band over the range of 200–300 K (maxima at ≈270 K) and 100–275 K (maxima at ≈208 K) in the GIG-CsPbBr₃:La³⁺ and GIG-CsPbBr₃:Lu³⁺ NCs, respectively. In comparison, there were no obvious TL signals in the GIG-CsPbBr₃ NCs. This indicates that the trapping levels are presented in these GIG-CsPbBr₃:Ln³⁺ systems. In this sense, by taking into account our theoretical DFT and experimental results, a mechanism (Figure 11) that can jointly explain why there is a PL blueshift (Figure 3b) and the transient PL intensity enhancement in the GIG-CsPbBr₃:Ln³⁺ NCs is established. If we excite, for instance, at 405 nm (i.e., ≈3.06 eV, which is in the absorption range of CsPbBr₃^[34,36,39]), an electron-hole pair that forms an exciton can be created in which the electron and the hole are bound by means of Coulomb interaction. This exciton can either recombine radiatively to generate a green emission (i.e., 2.43 eV, ≈510 nm, Figure 11b) or be dissociated in the case of charge trapping at defect sites that result from the Ln³⁺ doping (Figure 11a,c).

As we previously stated, the substitution of Pb²⁺ lattice sites with smaller Lu³⁺ and La³⁺ ions leads to a shrinkage of the CsPbBr₃ cell lattice. Meanwhile, the more the Pb²⁺ ions are

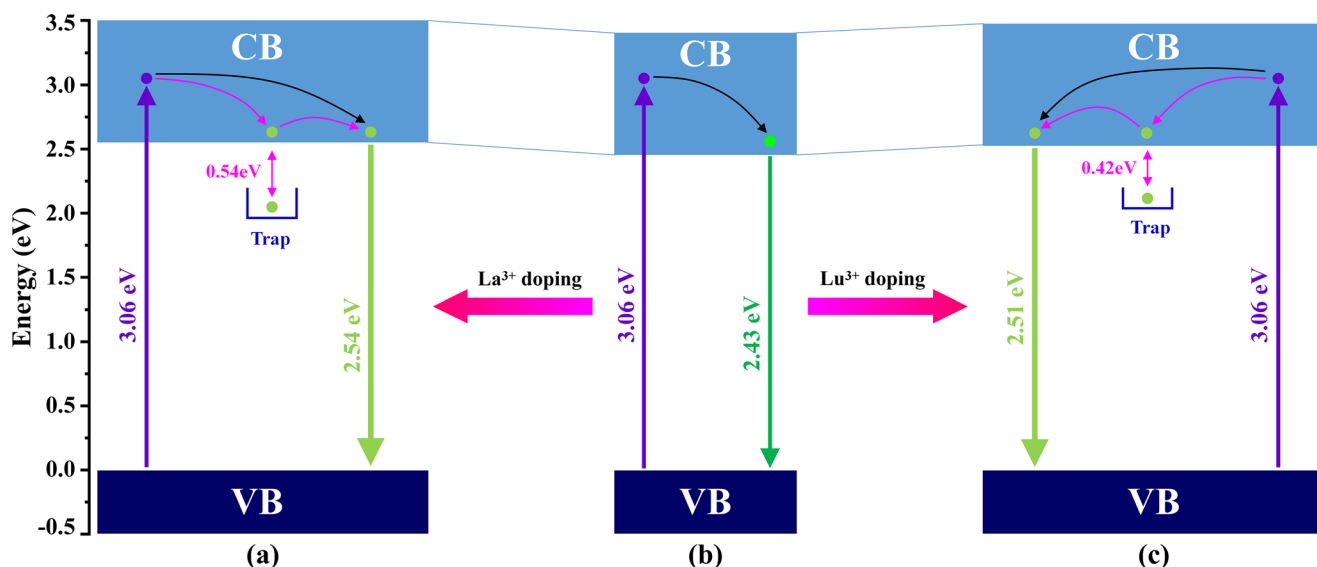


Figure 11. Mechanism explaining both the spectral tuning depicted in Figure 3 and the spontaneous PL intensity enhancement observed in Figure 10. a–c) CB and VB denote conduction band and valence band, respectively. Note that the trap depths of 0.54 and 0.42 eV in (a) and (c) are obtained based on the TL bands of La^{3+} and Lu^{3+} doped GIG-CsPbBr₃ QDs very similar to our samples but with a doping rate of 0.6 %, [31] and the equation used is $T = T_m/500$, where E is the trap depth, T_m denotes the temperature of the glow peak and the unit of constant is 500 K eV⁻¹. [104]

replaced by the Lu^{3+} and La^{3+} ions, the more the cell lattice shrinks and the larger E_g values will be. Accordingly, an expansion of E_g (i.e., the energy separating the VB top to the CB bottom) appears, leading to a shift of the emission positions to high energies with the increase of the La^{3+} and Lu^{3+} doping rates. Since there are trapping states that are located below the CB bottom to serve as electron traps or above the VB top to serve as hole traps, the trapped carriers can be detrapped from these traps with the assistance of laser irradiation. In this case, coupled with those without being captured by the traps, the laser irradiation-induced detrapping of the trapped carriers and their subsequent radiative recombination contribute to the total PL output. Therefore, the observed spontaneous PL intensity enhancement is ascribed to the thermal and/or photo-stimulated detrapping of charge carriers captured at the defect sites that result from the Ln^{3+} doping and their subsequent radiative recombination that reinforces the PL intensity. However, once the trapped carriers are emptied without a further supplement, the enhanced PL intensity cannot sustain, even though we continued to perform the laser irradiation on the GIG-samples. On the other hand, due to the existence of the Ln^{3+} doping-induced defects like Br^- -related defects, the PL intensity can be partially recovered in the GIG-CsPbBr₃:1.1% La^{3+} and GIG-CsPbBr₃:1.1% Lu^{3+} NCs (the blue points in Figure 10b,c(ii)) after tuning off the laser and then staying in the dark for 18 and 20 h, respectively.

Moreover, very likely due to a slow supplement of the electrons in the dark environment, the PL self-recovery process is slow, but as depicted by the purple points in Figure 7b(ii), it can speed up with the help of an artificial halogen lamp light. By contrast, because the GIG-CsPbBr₃ NCs do not involve the Ln^{3+} doping and the corresponding Ln^{3+} -doping induced defects, they do not show the PL intensity enhancement, no matter how long time they are exposed to a 405 nm laser light irradiation. An inspection of Figure 10a(ii) reveals that the GIG-CsPbBr₃ NCs can slowly

recover 6.5% of the initial PL intensity after staying in the dark for 20 h. This is possibly due to other defects (e.g., surface or oxygen) that are generated in the glass formation process. Therefore, the GIG-CsPbBr₃ NCs that stayed in the dark for the same time of, such as, ≈ 20 h, show a PL intensity recovery rate that is slower than the GIG-CsPbBr₃:1.1% Lu^{3+} NCs. With this logical deduction, such PL difference concludes the potential existence of the Ln^{3+} doping-induced defects that help to speed up the PL recovery.

4.5. Warm-White Emitting Prototype

Normally, artificial white light is realized by additively mixing the emissions from red, green, and blue (i.e., tricolors) LED chips or by combining multiple color-emitting or single white-emitting materials with a UV/blue LED chip or laser. [5,56–58,66,69,70,89,98,99,103,104] The most desirable white light should feature low risk (e.g., no serious UV light leakage), high CRI and low CCT values, as well as an emitted white light perception as close as possible to natural sunlight (i.e., warm white). Following these guidelines, we have designed a prototype by a direct blend of the light from a 405 nm laser, green light from GIG-CsPbBr₃ powders (i.e., not monolithic glass), yellow light from commercial YAG:Ce³⁺ phosphor, and red light from the CaWO₄:Eu³⁺ phosphor. The fabrication profile for this white prototype and the normalized PL spectra of the four-color components are shown in Figure 12a,b. After a direct blend of ≈ 33.9 wt% of green GIG-CsPbBr₃ powders (≈ 1 g), ≈ 30.5 wt% of yellow YAG:Ce³⁺ (≈ 0.9 g) and ≈ 35.6 wt% of red CaWO₄:Eu³⁺ (≈ 1.05 g) phosphors and then irradiation with a 405 nm laser having the power output of 1 mW, a warm white-emitting prototype, with a CIE chromaticity coordinate at (0.4110, 0.3706) (Figure 12c), a CRI of 89, and a CCT of 3363 K, is achieved. The PL spectrum

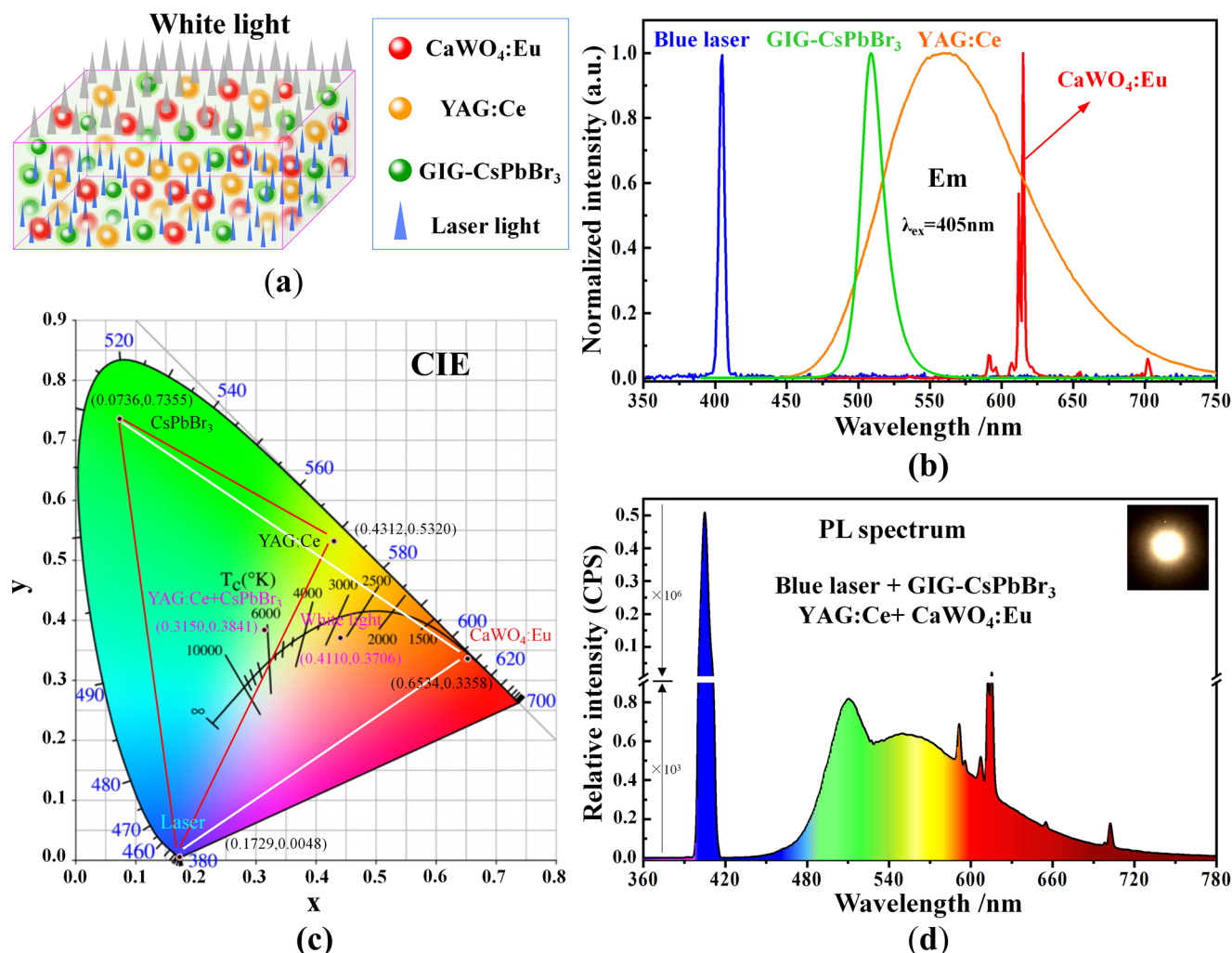


Figure 12. a) Design concept of a near-warm white light-emitting prototype through combining the light of a 405 nm laser with the emissions from green $\text{GIG}-\text{CsPbBr}_3$ powders, yellow $\text{YAG}:\text{Ce}$ and red $\text{CaWO}_4:\text{Eu}^{3+}$ phosphors. b) Normalized PL spectra of the four components of the 405 nm laser light, and the green $\text{GIG}-\text{CsPbBr}_3$ powders, red $\text{CaWO}_4:\text{Eu}^{3+}$ and yellow $\text{YAG}:\text{Ce}$ phosphors upon irradiation with a 405 nm laser. c) CIE chromaticity coordinates calculated based on the PL spectra of (b). d) PL spectra and digital photo (inset) of a 405 nm laser-converted near-warm white light-emitting prototype, where the corresponding CIE value is shown in (c). Note that the $\text{GIG}-\text{CsPbBr}_3$ powders, $\text{YAG}:\text{Ce}^{3+}$ and $\text{CaWO}_4:\text{Eu}^{3+}$ phosphors are first mixed for ≈ 30 min in an agate mortar, and then passed through a 500-mesh sieve to obtain the relatively uniform yet multicolors-emitting powders.

of this warm-white emitting prototype together with its digital photo is exhibited in Figure 12d. Clearly, these preliminary results vividly demonstrate the attractiveness of MHPs-typed $\text{GIG}-\text{CsPbBr}_3$ for use in the laser-converted white lighting and display technology.

5. Conclusion and Perspectives

In summary, we have succeeded in achieving MHPs-typed $\text{GIG}-\text{CsPbBr}_3$ and $\text{GIG}-\text{CsPbBr}_3:\text{Ln}^{3+}$ ($\text{Ln} = \text{La}$, or Lu) NCs through an in situ nanocrystallization method. Upon excitation with a 405 nm laser, a gradual shift of PL positions from 510.6 nm to 488.0 nm in the $\text{GIG}-\text{CsPbBr}_3:\text{La}^{3+}$ and 510.6 to 493.5 nm in the $\text{GIG}-\text{CsPbBr}_3:\text{Lu}^{3+}$ is achieved as the La^{3+} and Lu^{3+} doping rates are increased from 0 to 1.3%. This blueshift of emission positions is confirmed under a 375 nm laser excitation. Our DFT calculations reveal that the replacement of Pb^{2+} lattice sites with,

for instance, trivalent La^{3+} ions, brings about the shrinkage of CsPbBr_3 lattice parameters and, after considering the presence of Br^- -related defects, leads to a continuous enlargement of the optical bandgap that accounts for the blueshift of PL positions. Our experimental results pertaining to the PL behaviors under various exposures including moisture, strong acid–base solutions, repeated heating–cooling cycles, and laser light irradiation, show that the $\text{GIG}-\text{CsPbBr}_3$ and $\text{GIG}-\text{CsPbBr}_3:\text{Ln}^{3+}$ NCs sustain much better PL properties than the $\text{GU}-\text{CsPbBr}_3$ NCs. All the GIG samples show partial or total recovery of their PL intensity and peak positions either after they are repeatedly heated and cooled in the order of $-150^\circ\text{C} \leftrightarrow -70^\circ\text{C} \leftrightarrow 20^\circ\text{C} \leftrightarrow 70^\circ\text{C} \leftrightarrow 150^\circ\text{C}$ for 30 cycles, or exposed to a 405 nm laser irradiation for a long term. Meanwhile, they preserve $>67\%$, $>58\%$, and $>80\%$ of their initial PL intensity in water at RT for 300 days, in boiled water for 12 h, and in corrosive solution environments in the range of pH values from 4 to 12 for 12 h, respectively. In particular, a spontaneous en-

hancement of 20–25% of the PL intensity during the first stage of a 405 nm laser irradiation is observed in the GIG-CsPbBr₃:Ln³⁺ NCs. Based on the observed PL information, the DFT calculations, the CsPbBr₃ structural features, the lattice variation caused by the Ln³⁺ dopants, and the borosilicate-based matrix properties, the spontaneous enhancement of the PL intensity is assigned to the presence of the defects-trapped electrons that result from the Ln³⁺ doping-induced defects and the subsequent radiative recombination of charge carriers that are detrapped from trapping levels upon the laser irradiation and that then reinforce the PL intensity spontaneously. Finally, a warm-white emitting prototype, with a CIE chromaticity coordinate at (0.4110, 0.3706), high CRI of 89, and low CCT of 3363 K, is realized by combining the light of a 405 nm laser with the emissions from green GIG-CsPbBr₃ NCs powders, yellow YAG:Ce and red CaWO₄:Eu³⁺ phosphors.

However, since the glass-related systems are always complicated, a further “in-depth” study, such as an experiment combining the in situ time-resolved X-ray diffraction used by Kirschner et al.,^[105] the electron paramagnetic resonance or electron spin resonance spectroscopy with the theoretical DFT calculations needs to be carried out, in order to verify whether or not, for instance, there is a reversible transition between the cubic phase or other phases like orthorhombic phase when the GIG-MHPs-typed NCs are exposed to the repeated heating-cooling experiments and a continuous laser light irradiation, and a reduction in surface and/or interface states in the glass that can contribute to the spectral shift and the enhanced PL intensity, as well as how other surface or defects/vacancies that are generated during the glass formation process affect the PL properties since the borosilicates-based glass matrix itself consists of many other elements like B, Si, Zn, Sr, and O. Furthermore, we show the contribution of Ln³⁺-doping induced Br[−]-related defects to the PL shift, and conclude that the spontaneous enhancement of PL intensity is due to the existence of defects-induced trapping states that can be released from defects. However, we know that they result from the Ln³⁺ doping, but the real nature of the traps responsible for this enhanced PL intensity is still unclear, which needs a further study. Nevertheless, in the present work we have not only succeeded in realizing the PL-tuning in the GIG-CsPbBr₃ NCs by doping external nonluminescent La³⁺ and Lu³⁺ ions, but also illustrated the importance of glass protection in retaining the PL stability of MHPs-typed GIG-CsPbBr₃ NCs. Furthermore, based on the observed PL information, the DFT calculation and some previous results like the thermoluminescence, we have proposed a mechanistic profile that can be used to explain both the PL-tuning and the spontaneous PL intensity enhancement. Meanwhile, we also demonstrate new potential opportunities of MHPs-typed GIG-NCs towards laser lighting technology.

Acknowledgements

F.K. and Y.D. contributed equally to this work. In this work, F.K. thanks for the financial support of the European Union's Seventh framework programme (FP7) and Horizon 2020 research and innovation program (H2020, No. 609405) under the Marie Skłodowska-Curie grant (grant no. 713683) (COFUNDfellowsDTU), the “Spring Buds Talent” Program and the starting grant from Ningbo Institute of Materials Technology and Engineering (NIMTE) Chinese Academy of Sciences (CAS), and the “Double Hundred Talent” project and the starting grant from Sichuan University. Y.D. thanks the financial support of the National Science Foundation of

China for Youth (Grant No. 11804160). M.W. acknowledges the support by the Danish National Research Foundation through NanoPhoton - Center for Nanophotonics, Grant No. DNRF147 and Center for Nanostructured Graphene, Grant No. DNRF103, and by the Independent Research Fund Denmark - Natural Sciences (Project No. 0135-00403B). K.Z. thanks the financial support from the Independent Research Fund Denmark-Sapere Aude starting grant (Project No. 7026-00037A), and Swedish Research Council VR starting grant (Project No. 201705337). The TEM measurements were supported by DTU Nanolab, the National Centre for Nano Fabrication and Characterization at the Technical University of Denmark (DTU). All the authors are also very grateful to the anonymous reviewers who raised useful and helpful comments to this work.

Conflict of Interest

The authors declare no conflict of interest.

Data Availability Statement

The data that support the findings of this study are available on request from the corresponding author. The data are not publicly available due to privacy or ethical restrictions.

Keywords

CsPbBr₃, glass, laser lighting, luminescence sustainability and enhancement, spectral tuning

Received: March 12, 2022

Revised: August 6, 2022

Published online:

- [1] W. Li, Z. M. Wang, F. Deschler, S. Gao, R. H. Friend, A. K. Cheetham, L. Ortega-San-Martin, *Nat. Rev. Mater.* **2017**, *2*, 16099.
- [2] M. D. Smith, B. A. Connor, H. I. Karunadasa, *Chem. Rev.* **2019**, *119*, 3104.
- [3] J. S. Manser, J. A. Christians, P. V. Kamat, *Chem. Rev.* **2016**, *116*, 12956.
- [4] C. Z. Ning, L. T. Dou, P. D. Yang, *Nat. Rev. Mater.* **2017**, *2*, 17070.
- [5] Y. Wei, Z. Y. Cheng, J. Lin, *Chem. Soc. Rev.* **2019**, *48*, 310.
- [6] F. Igbari, Z. K. Wang, L. S. Liao, *Adv. Energy Mater.* **2019**, *9*, 1803150.
- [7] S. Vasala, M. Karppinen, *Prog. Solid State Chem.* **2015**, *43*, 1.
- [8] Y. X. Zhao, K. Zhu, *Chem. Soc. Rev.* **2016**, *45*, 655.
- [9] F. Dogan, H. Lin, M. Guilloux-Viry, O. Peña, *Sci. Technol. Adv. Mater.* **2015**, *16*, 020301.
- [10] J. Shamsi, A. S. Urban, M. Imran, L. De Trizio, L. Manna, *Chem. Rev.* **2019**, *119*, 3296.
- [11] H. W. Lian, Y. Li, K. Sharafudeen, W. R. Zhao, G. R. Krishnan, S. A. Zhang, J. R. Qiu, K. Huang, G. Han, *Adv. Mater.* **2020**, *32*, 2002495.
- [12] Y. S. Xu, X. D. Zhao, M. L. Xia, X. H. Zhang, *J. Mater. Chem. C* **2021**, *9*, 5452.
- [13] Q. S. Chen, J. Wu, X. Y. Ou, B. L. Huang, J. Almutlaq, A. A. Zhumekenov, X. W. Guan, S. Y. Han, L. L. Liang, Z. G. Yi, J. Li, X. J. Xie, Y. Wang, Y. Li, D. Y. Fan, D. B. L. The, A. H. Ali, O. F. Mohammed, O. M. Bakr, T. Wu, M. Bettinelli, H. H. Yang, W. Huang, X. G. Liu, *Nature* **2018**, *561*, 88.
- [14] S. Q. Lou, T. T. Xuan, C. Y. Yu, M. M. Cao, C. Xia, J. Wang, H. L. Li, *J. Mater. Chem. C* **2017**, *5*, 7431.
- [15] S. C. Hou, Y. Z. Guom, Y. G. Tang, Q. M. Quan, *ACS Appl. Mater. Interfaces* **2017**, *9*, 18417.

- [16] Q. X. Zhong, M. H. Cao, H. C. Hu, D. Yang, M. Chen, P. L. Li, L. Z. Wu, Q. Zhang, *ACS Nano* **2018**, *12*, 8579.
- [17] J. Cai, K. L. Gu, Y. H. Zhu, J. R. Zhu, Y. W. Wang, J. H. Shen, A. Trinch, C. Z. Li, G. Wei, *Chem. Commun.* **2018**, *54*, 8064.
- [18] B. B. Yang, F. Zheng, S. L. Mei, Z. H. Chen, Y. Xie, H. Q. Dai, X. Wei, W. L. Zhang, F. X. Xie, J. Q. Ju, Y. Q. Chu, J. Zou, R. Q. Guo, *Appl. Surf. Sci.* **2020**, *512*, 145655.
- [19] M. Kazes, T. Udayabhaskararao, S. Dey, D. Oron, *Acc. Chem. Res.* **2021**, *54*, 1409.
- [20] B. A. Koscher, J. K. Swabeck, N. D. Bronstein, A. P. Alivisatos, *J. Am. Chem. Soc.* **2017**, *139*, 6566.
- [21] D.-H. Kang, S. R. Pae, J. Shim, G. Yoo, J. Jeon, J. W. Leem, S. J. Yu, S. Lee, B. Shin, J. H. Park, *Adv. Mater.* **2016**, *28*, 7799.
- [22] N. Rajamanickam, P. Soundararajan, S. M. Senthil Kumar, K. Jayakumar, K. Ramachandran, *Electrochim. Acta* **2019**, *296*, 771.
- [23] S. R. Li, J. Luo, J. Liu, J. Tang, *J. Phys. Chem. Lett.* **2019**, *10*, 1999.
- [24] Z. L. Zhang, L. L. Shen, H. L. Zhang, L. Ding, G. S. Shao, X. J. Liang, W. D. Xiang, *Chem. Eng. J.* **2019**, *378*, 122125.
- [25] M. L. Xia, S. J. Zhu, J. J. Luo, Y. S. Xu, P. F. Tian, G. D. Niu, J. Tang, *Adv. Opt. Mater.* **2021**, *9*, 2002239.
- [26] Y. F. Hu, S. Kareem, H. Dong, W. Xiong, S. Q. Tian, J. Shamsi, L. Li, X. J. Zhao, Y. Xie, *ACS Appl. Nano Mater.* **2021**, *4*, 6306.
- [27] Y. Y. Duan, C. Ezquerro, E. Serrano, E. Lalinde, J. García-Martínez, J. R. Berenguer, R. D. Costa, *Adv. Funct. Mater.* **2020**, *30*, 2005401.
- [28] H. C. Wang, S. Y. Lin, A. C. Tang, B. P. Singh, H. C. Tong, C. Y. Chen, Y. C. Lee, T. L. Tsai, R. S. Liu, *Angew. Chem., Int. Ed.* **2016**, *55*, 7924.
- [29] Y. L. Wei, E.-H. Heike, J. B. Zhao, *Adv. Opt. Mater.* **2019**, *7*, 1900702.
- [30] I. Konidakis, A. Karagiannaki, E. Stratakis, *Nanoscale* **2022**, *14*, 2966.
- [31] X. J. Huang, Q. Y. Guo, D. D. Yang, X. D. Xiao, X. F. Liu, Z. G. Xia, F. J. Fan, J. R. Qiu, G. P. Dong, *Nat. Photonics* **2020**, *14*, 82.
- [32] X. J. Huang, Q. Y. Guo, S. L. Kang, T. C. Ouyang, Q. P. Chen, X. F. Liu, Z. G. Xia, Z. M. Yang, Q. Y. Zhang, J. R. Qiu, G. P. Dong, *ACS Nano* **2020**, *14*, 3150.
- [33] S. Yuan, D. Q. Chen, X. Y. Li, J. S. Zhong, X. H. Xu, *ACS Appl. Mater. Interfaces* **2018**, *10*, 18918.
- [34] H. Zhang, Z. Yang, L. Zhao, J. Y. Cao, X. Yu, Y. Yang, S. F. Yu, J. B. Qiu, X. H. Xu, *Adv. Opt. Mater.* **2020**, *8*, 2000585.
- [35] J. Kang, L. J. Wang, *Phys. Chem. Lett.* **2017**, *8*, 489.
- [36] L. Protesescu, S. Yakunin, M. I. Bodnarchuk, F. Krieg, R. Caputo, C. H. Hendon, R. Y. Yang, A. Walsh, M. V. Kovalenko, *Nano Lett.* **2015**, *15*, 3692.
- [37] Z. C. Zeng, Y. S. Xu, Z. S. Zhang, Z. S. Gao, M. Luo, Z. Y. Yin, C. Zhang, J. Xu, B. L. Huang, F. Luo, Y. P. Du, C. H. Yan, *Chem. Soc. Rev.* **2020**, *49*, 1109.
- [38] C.-H. Lu, G. B. Biesold-Mcgee, Y. J. Liu, Z. T. Kang, Z. Q. Lin, *Chem. Soc. Rev.* **2020**, *49*, 4953.
- [39] G. C. Pan, X. Bai, D. W. Yang, X. Chen, P. T. Jing, S. N. Qu, L. J. Zhang, D. L. Zhou, J. Y. Zhu, W. Xu, B. Dong, H. W. Song, *Nano Lett.* **2017**, *17*, 8005.
- [40] D. Y. Huang, P. P. Dang, H. Z. Lian, Q. G. Zeng, J. Lin, *Inorg. Chem.* **2019**, *58*, 15507.
- [41] S. H. Zou, Y. S. Liu, J. H. Li, C. P. Liu, R. Feng, F. L. Jiang, Y. X. Li, J. Z. Song, H. B. Zeng, M. C. Hong, X. Y. Chen, *J. Am. Chem. Soc.* **2017**, *139*, 11443.
- [42] D. Manna, T. K. Das, A. Yella, *Chem. Mater.* **2019**, *31*, 10063.
- [43] A. Karmakar, M. S. Dodd, S. Agnihotri, E. Bavera, V. K. Michaelis, *Chem. Mater.* **2018**, *30*, 8280.
- [44] L. J. Huang, L. T. Lin, W. Xie, Z. C. Qiu, H. Y. Ni, H. B. Liang, Q. Tang, L. W. Cao, J.-X. Meng, F. Y. Li, *Chem. Mater.* **2020**, *32*, 5579.
- [45] G. C. Pan, X. Bai, W. Xu, X. Chen, Y. Zhai, J. Y. Zhu, H. Shao, N. Ning, L. Xu, B. Dong, Y. L. Mao, H. W. Song, *ACS Appl. Mater. Interfaces* **2020**, *12*, 14195.
- [46] G. C. Adhikari, S. Thapa, H. Y. Zhu, P. F. Zhu, *Adv. Opt. Mater.* **2019**, *7*, 1900916.
- [47] X. Y. Shen, Y. Zhang, S. V. Kershaw, T. S. Li, C. C. Wang, X. Y. Zhang, W. Y. Wang, D. G. Li, Y. H. Wang, M. Lu, L. J. Zhang, C. Sun, D. Zhao, G. S. Qin, X. Bai, W. W. Yu, A. L. Rogach, *Nano Lett.* **2019**, *19*, 1552.
- [48] D. D. Xu, Q. Zhang, X. M. Wu, W. W. Li, J. X. Meng, *Mater. Res. Bull.* **2019**, *110*, 135.
- [49] A. Biswas, R. Bakthavatsalam, J. Kundu, *Chem. Mater.* **2017**, *29*, 7816.
- [50] F. Y. Zhao, Z. Song, J. Zhao, Q. L. Liu, *Inorg. Chem. Front.* **2019**, *6*, 3621.
- [51] A. K. Guria, S. K. Dutta, S. Das Adhikari, N. Pradhan, *ACS Energy Lett.* **2017**, *2*, 1014.
- [52] Y. Q. Zhang, J. M. Liu, H. L. Zhang, Q. Y. He, X. J. Liang, W. D. Xiang, *J. Eur. Ceram. Soc.* **2020**, *40*, 6023.
- [53] K. Y. Xu, A. Meijerink, *Chem. Mater.* **2018**, *30*, 5346.
- [54] B. B. Su, M. S. Molokeev, Z. G. Xia, *J. Phys. Chem. Lett.* **2020**, *11*, 2510.
- [55] R. Begum, M. R. Parida, A. L. Abdelhady, B. Murali, N. M. Alyami, G. H. Ahmed, M. N. Hedhili, O. M. Bakr, O. F. Mohammed, *J. Am. Chem. Soc.* **2017**, *139*, 731.
- [56] Y. Z. Cheng, C. Y. Shen, L. L. Shen, W. D. Xiang, X. J. Liang, *ACS Appl. Mater. Interfaces* **2018**, *10*, 21434.
- [57] F. W. Kang, M. Y. Peng, Q. Y. Zhang, J. R. Qiu, *Chem. - Eur. J.* **2014**, *20*, 11522.
- [58] F. W. Kang, Y. Zhang, M. Y. Peng, *Inorg. Chem.* **2015**, *54*, 1462.
- [59] Y. M. Zhao, C. Riemersma, F. Pietra, R. Koole, C. de Mello Donegà, A. Meijerink, *ACS Nano* **2012**, *6*, 9058.
- [60] J. S. Chen, D. Z. Liu, M. J. Al-Marri, L. Nuuttila, H. Lehtivuori, K. B. Zheng, *Sci. China Mater.* **2016**, *59*, 719.
- [61] J. S. Chen, K. Židek, P. Chábera, D. Z. Liu, P. F. Cheng, L. Nuuttila, M. J. Al-Marri, H. Lehtivuori, M. E. Messing, K. L. Han, K. B. Zheng, T. Pullerits, *J. Phys. Chem. Lett.* **2017**, *8*, 2316.
- [62] G. Kresse, J. Hafner, *Phys. Rev. B* **1993**, *47*, 558.
- [63] G. Kresse, J. Joubert, *Phys. Rev. B: Condens. Matter Mater. Phys.* **1999**, *59*, 1758.
- [64] J. P. Perdew, K. Burke, M. Ernzerhof, *Phys. Rev. Lett.* **1996**, *77*, 3865.
- [65] C. B. Yang, B. Zhuang, J. D. Lin, S. X. Wang, M. L. Liu, N. Z. Jiang, D. Q. Chen, *Chem. Eng. J.* **2020**, *398*, 125616.
- [66] X. X. Di, Z. M. Hu, J. T. Jiang, M. L. He, L. Zhou, W. D. Xiang, X. J. Liang, *Chem. Commun.* **2017**, *53*, 11068.
- [67] R. R. Yuan, L. L. Shen, C. Y. Shen, J. M. Liu, L. Zhou, W. D. Xiang, X. J. Liang, *Chem. Commun.* **2018**, *54*, 3395.
- [68] D. Q. Chen, S. Yuan, X. Chen, J. N. Li, Q. N. Mao, X. Y. Li, J. S. Zhong, *J. Mater. Chem. C* **2018**, *6*, 6832.
- [69] D. Q. Chen, S. Yuan, J. K. Chen, J. S. Zhong, X. H. Xu, *J. Mater. Chem. C* **2018**, *6*, 12864.
- [70] Y. Ye, W. C. Zhang, Z. Y. Zhao, J. Wang, C. Liu, Z. Deng, X. J. Zhao, J. J. Han, *Adv. Opt. Mater.* **2019**, *7*, 1801663.
- [71] L. Ding, S. N. Liu, Z. L. Zhang, G. Z. Shao, W. D. Xiang, X. J. Liang, *Ceram. Int.* **2019**, *45*, 22699.
- [72] P. P. Li, W. Q. Xie, W. Mao, Y. Tian, F. F. Huang, S. Q. Xu, J. J. Zhang, *J. Mater. Chem. C* **2020**, *8*, 473.
- [73] X. L. Pang, H. R. Zhang, L. Q. Xie, T. T. Xuan, Y. Q. Sun, S. C. Si, B. Jiang, W. B. Chen, J. L. Zhuang, C. F. Hu, Y. L. Liu, B. F. Lei, X. J. Zhang, *J. Mater. Chem. C* **2019**, *7*, 13139.
- [74] X. Z. Zhang, L. Z. Guo, Y. H. Zhang, C. H. Cheng, Y. Cheng, X. P. Li, J. S. Zhang, S. Xu, Y. Z. Cao, J. S. Sun, L. H. Cheng, B. J. Chen, *J. Am. Ceram. Soc.* **2020**, *103*, 5028.
- [75] H. L. Zhang, L. Yuan, Y. Chen, Y. Q. Zhang, Y. X. Yu, X. J. Liang, W. D. Xiang, T. Wang, *Chem. Commun.* **2020**, *56*, 2853.
- [76] E. H. Cao, J. B. Qiu, D. C. Zhou, Y. Yang, Q. Wang, Y. G. Wen, *Chem. Commun.* **2020**, *56*, 4460.
- [77] Y. X. Zhu, B. B. Yang, Q. Lu, Y. Li, M. M. Shi, J. Zou, *ECSJ. Solid State Sci. Technol.* **2020**, *9*, 126003.
- [78] S. S. Li, L. J. Nie, S. M. Ma, G. P. Yao, F. M. Zeng, X. Y. Wang, C. Y. Sun, G. X. Hu, Z. M. Su, *J. Eur. Ceram. Soc.* **2020**, *40*, 3270.

- [79] H. L. Zhang, R. R. Yuan, M. F. F. Jin, Z. L. Zhang, Y. X. Yu, W. D. Weidong Xiang, X. J. Liang, *J. Eur. Ceram. Soc.* **2020**, *40*, 94.
- [80] B. W. Zhang, K. Zhang, L. F. Li, C. C. Xu, R. F. Wang, C. Wang, J. Yang, Y. Yang, Y. Wang, J. Wang, F. Qiu, T. Sun, C. H. Zhou, X. M. Wen, *J. Alloys Compd.* **2021**, *874*, 159962.
- [81] S. S. Lin, H. Lin, G. X. Chen, B. Wang, X. M. Yue, Q. G. Huang, J. Xu, Y. Cheng, Y. S. Wang, *Laser Photonics Rev.* **2021**, *15*, 2100044.
- [82] P. P. Li, Y. M. Duan, Y. Lu, A. Xiao, Z. Y. Zeng, S. Q. Xu, J. J. Zhang, *Nanoscale* **2020**, *12*, 6630.
- [83] Y. Lu, P. P. Li, W. Q. Xie, Y. M. Duan, S. Q. Xu, J. J. Zhang, *Opt. Lett.* **2021**, *46*, 2597.
- [84] Y. Tong, Q. Wang, H. Yang, X. T. Liu, E. R. Mei, X. J. Liang, Z. J. Zhang, W. D. Xiong, *Photonics Res.* **2021**, *9*, 2369.
- [85] E. Erol, O. Kibrisli, M. Ç. Ersundu, A. E. Ersundu, *Phys. Chem. Chem. Phys.* **2022**, *24*, 1486.
- [86] X. L. Tian, R. F. Wei, Z. J. Ma, J. R. Qiu, *Adv. Opt. Mater.* **2022**, *10*, 2102483.
- [87] X. Q. Xiang, H. Lin, R. F. Li, Y. Cheng, Q. M. Huang, J. Xu, C. Y. Wang, X. Y. Chen, Y. S. Wang, *Nano Res.* **2019**, *12*, 1049.
- [88] Z. H. Wang, Y. M. Duan, P. P. Li, S. Q. Xu, J. J. Zhang, *J. Lumin.* **2022**, *250*, 118918.
- [89] L. Niu, H. Shi, Y. Ye, C. Liu, B. N. Jia, Y. S. Chu, L. Liu, J. Ren, J. Z. Zhang, *J. Non-Cryst. Solids* **2022**, *581*, 121429.
- [90] Y. D. Zhang, W. C. Zhang, Y. Ye, K. Li, X. Gong, C. Liu, *Sol. Energy Mater. Sol. Cells* **2022**, *238*, 111619.
- [91] Y. Yuan, R. Xu, H. T. Xu, F. Hong, F. Xu, L.-J. Wang, *Chin. Phys. B* **2015**, *24*, 116302.
- [92] M. Ahmad, G. Rehman, L. Ali, M. Shafiq, R. I. R. Ahmad, T. Khan, S. Jalali-Asadabadi, M. Maqbool, I. Ahmad, *J. Alloys Compd.* **2017**, *705*, 828.
- [93] A. Amat, E. Mosconi, E. Ronca, C. Quarti, P. Umari, M. K. Nazeeruddin, G. Michael, F. De Angelis, *Nano Lett.* **2014**, *14*, 3608.
- [94] F. W. Kang, X. B. Yang, M. Y. Peng, L. Wondraczek, Z. J. Ma, Q. Y. Zhang, J. R. Qiu, *J. Phys. Chem. C* **2014**, *118*, 7515.
- [95] H. S. Zhang, F. W. Kang, Y. J. Zhao, M. Y. Peng, D. Y. Lei, X. B. Yang, *J. Mater. Chem. C* **2017**, *5*, 314.
- [96] Z. Yang, L. Zhao, M. X. Li, Q. H. Yang, Z. H. Fang, L. L. Yang, X. Yu, J. B. Qiu, Y. Yang, X. H. Xu, *J. Am. Ceram. Soc.* **2020**, *103*, 4150.
- [97] D. Malyshev, V. Sereda, I. Ivanov, M. Mazurin, A. Sednev-Lugovets, D. Tsvetkov, A. Zuev, *Mater. Lett.* **2020**, *278*, 128458.
- [98] S. H. You, S. X. Li, L. Wang, T. Takeda, N. Hirotsaki, R.-J. Xie, *Chem. Eng. J.* **2021**, *404*, 126575.
- [99] S. Li, L. Wang, N. Hirotsaki, R.-J. Xie, *Laser Photonics Rev.* **2018**, *12*, 1800173.
- [100] X. L. Zhang, F. B. Wang, B. B. Zhang, G. Q. Zha, W. Q. Jie, *Cryst. Growth Des.* **2020**, *20*, 4585.
- [101] J. H. Lee, N. C. Bristowe, J. H. Le, S. H. Lee, P. D. Bristowe, A. K. Cheetham, H. M. Jang, *Chem. Mater.* **2016**, *28*, 4259.
- [102] R. Prasanna, G.-P. Aryeh, L. Tomas, C. Bert, B. Aslihan, B. Hans-Gerd, F. T. Michael, D. M. Michael, *J. Am. Chem. Soc.* **2017**, *139*, 11117.
- [103] N. Kimura, K. Sakuma, S. Hirafune, K. Asano, N. Hirotsaki, R. J. Xie, *Appl. Phys. Lett.* **2007**, *90*, 051109.
- [104] Z. L. Zhang, L. L. Shen, H. L. Zhang, L. Ding, G. Z. Shao, X. J. Liang, W. D. Xiang, *Chem. Eng. J.* **2019**, *378*, 122125.
- [105] M. S. Kirschner, B. T. Diroll, P. J. Guo, S. M. Harvey, W. Helweh, N. C. Flanders, A. Brumberg, N. E. Watkins, A. A. Leonard, A. M. Evans, M. R. Wasielewski, W. R. Dichtel, X. Y. Zhang, L. X. Chen, R. D. Schaller, *Nat. Commun.* **2019**, *10*, 504.